Flying-V Family

Design for Stability & Control

M.R. van der Toorn

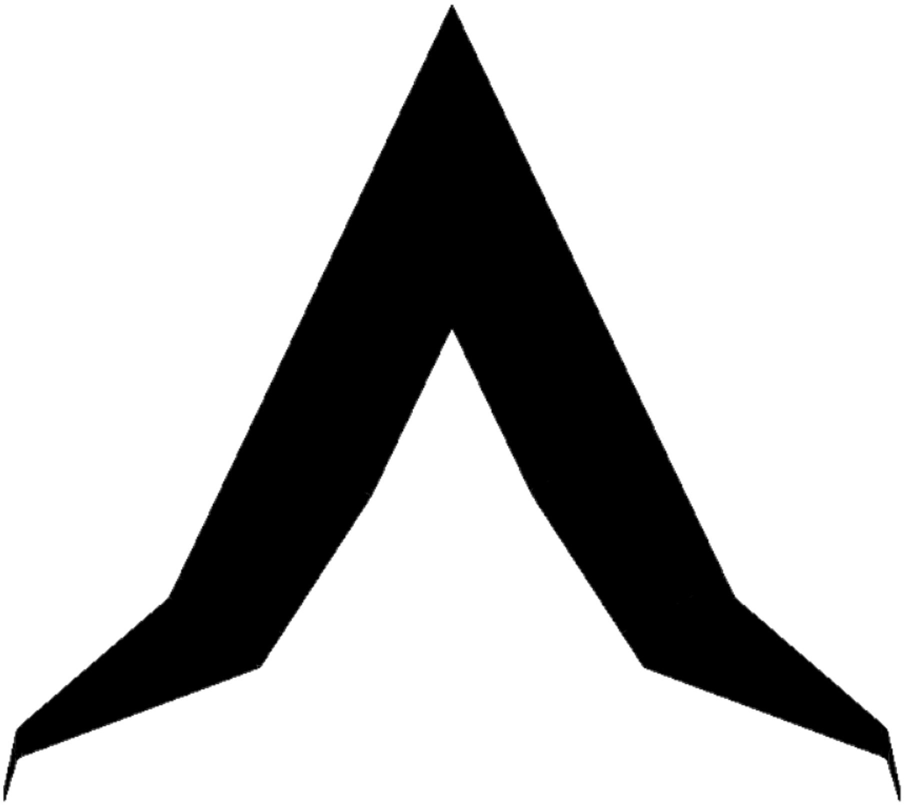

TU Delft

Flying-V Family

Design for Stability & Control

by

M.R. van der Toorn

to obtain the degree of Master of Science
at the Delft University of Technology,
to be defended publicly on Wednesday April 20, 2022 at 9:30 AM.

Student number:	4350723	
Project duration:	October 18, 2021 - April 20, 2022	
Thesis committee:	Dr. ir. R. Vos,	TU Delft, supervisor
	Prof. dr. ir. P. Colonna,	TU Delft
	Dr. ing. S. G. P. Castro	TU Delft

An electronic version of this thesis is available at `http://repository.tudelft.nl/`.

TU Delft

Abstract

The Flying-V is a novel aircraft configuration which promises better fuel efficiency than the current state of the art in commercial passenger transport. The main contributing factor to this accomplishment is its small wetted area relative to the available volume. Three family variants carrying different numbers of passengers are designed simultaneously. The airplane has elevons and rudders serving as control surfaces for trim and maneuvering. The Flying-V has been optimized for aerodynamic efficiency in previous research, but stability and control constraints have not yet been considered in detail. To find the effect of stability and control on the design variables and performance, an aerodynamic solver, mass distribution model, and control authority simulation have been established. The mass distribution model can be used to find the center of gravity and moment of inertia in any loading scenario. A strategy for fuel distribution for minimum CG travel is proposed. An optimization is performed using SciPy optimization tools. Planform geometry is used as the design vector. The design constraints include geometric contraints like maximum span and fuel capacity, and stability and control constraints like control authority for pitch, roll, and yaw maneuvers and static stability. The results of the optimization have shown that the stability and control constraints can be satisfied without a large fuel burn penalty (less than one percent) and stability and control constraints are not driving as long as the fins are large enough to accommodate rudders that provide sufficient directional control power. An optimized design that meets all requirements has a shorter outer wing, shorter fuselage, longer fins, and smaller outer wing sweep compared to the initial design. For the three optimized aircraft, the acceptable range of center of gravity is bounded by longitudinal stability and control requirements. The distribution of passenger and cargo weight in combination with the active fuel distribution system should be such that the CG during flight stays within these bounds. This is shown to be the case for the design payload configuration.

Preface

The document before you serves as the final deliverable to obtain a Master's degree in the field of aerospace engineering. It is also a result of months of work on a topic where the author could apply and demonstrate much of the knowledge gained in the past years. It has been exciting to work on the Flying-V project and to help bring it one step closer to take-off. I would like to thank my thesis supervisor Roelof Vos for giving me such an interesting topic to work on and for pointing me in the right direction when I encountered challenges.

I want to thank my family for their endless support and encouragement throughout my studies.

M.R. van der Toorn
Delft, April 2022

Contents

Abstract iii

List of Figures ix

List of Tables xi

Nomenclature xiii

1 Introduction 1
- 1.1 Research Objective . . . 1
- 1.2 Thesis Outline . . . 2

2 Background 3
- 2.1 Flying Wings . . . 3
- 2.2 Development of the Flying-V . . . 5
- 2.3 Stability and Control Considerations of the Flying-V . . . 6
- 2.4 Current Design . . . 7
  - 2.4.1 Top-level Requirements . . . 7
  - 2.4.2 Geometric Model and Parametrization. . . . 7
  - 2.4.3 Control Surfaces . . . 8
  - 2.4.4 Internal Layout . . . 9
- 2.5 ParaPy Framework . . . 9

3 Methodology 11
- 3.1 Multidisciplinary Design Optimization . . . 11
  - 3.1.1 Design Variables . . . 11
  - 3.1.2 Objective Function. . . . 13
  - 3.1.3 Constraints . . . 13
  - 3.1.4 Search Algorithm . . . 13
- 3.2 Aerodynamic Modelling. . . . 14
  - 3.2.1 VORLAX: A Vortex Lattice Solver . . . 14
  - 3.2.2 Viscous Drag Estimation . . . 16
- 3.3 Mass Distribution Estimation . . . 16
  - 3.3.1 Weight Estimation . . . 17
  - 3.3.2 Weight groups . . . 17
  - 3.3.3 Landing Gear and Engine Placement. . . . 19
  - 3.3.4 Passengers and Cargo Compartments . . . 19
  - 3.3.5 Fuel and Payload Loading Simulation . . . 20
- 3.4 Fuel Loading Strategy . . . 21
- 3.5 Cruise Performance Analysis . . . 24
- 3.6 Control Authority Assessment. . . . 25
  - 3.6.1 Longitudinal Trim . . . 25
  - 3.6.2 Pull-up Maneuver . . . 25
  - 3.6.3 Steady Sideslip . . . 26
  - 3.6.4 Engine-Out Trim . . . 26
  - 3.6.5 Time-to-Bank . . . 27
  - 3.6.6 Take-off Rotation. . . . 27
  - 3.6.7 Control Departure . . . 27
  - 3.6.8 Summary of Control Requirements . . . 28

4 Verification and Validation 31
4.1 Stability and Control Derivatives . . . 31
4.1.1 Comparison of Coefficients . . . 32
4.1.2 Correction Methods . . . 32
4.2 Weight Model Simplification . . . 35
4.3 Volume Estimation . . . 35
4.4 Moment of Inertia. . . . 37
4.5 Sensitivity Analysis . . . 38

5 Results 39
5.1 Optimization Results . . . 39
5.2 Effect of Loading Scenario . . . 42

6 Conclusions and Recommendations 49
6.1 Conclusions. . . . 49
6.2 Recommendations . . . 50

Bibliography 51

List of Figures

2.1 Horten Ho 229 prototype fighter. 3
2.2 B-2 Stealth Bomber employing split rudders for yaw control. 4
2.3 Flying-V concept top-view next to Airbus A350-900 including isometric view of the concept [1]. 5
2.4 Curve of moment coefficient around the center of gravity of the scaled Flying-V model for a range of elevon deflections [2]. CS1 and CS2 refer to the inboard and outboard elevons respectively. 6
2.5 Planform parametrization. 8
2.6 Cross-section parametrization. 8
2.7 Control surfaces on one side of the wing. 9
2.8 Floor plan layout of the FV-900. [3] 10

3.1 Optimization Architecture. All quantities in the grey blocks consist of three values: one for each aircraft family member. 12
3.2 Design variables. 12
3.3 Caption for LOF 15
3.4 VORLAX Representation of a Flying-V planform. 15
3.5 VORLAX Representation of a Flying-V isometric view. 15
3.6 Passenger cabin (red), cargo hold (green), and fuel tanks (yellow). 18
3.7 Solids representing the fuselage sections. 18
3.8 Solids and point masses of miscellaneous weight groups. Hydraulic and electric systems and paint are distributed over the whole wing. 19
3.9 Coordinate system and origin used to locate components. 20
3.10 Passengers (red), cargo (green), and fuel (yellow) in a specific loading scenario. 21
3.11 Loading diagram without active CG control. 23
3.12 Loading diagram with active CG control. 23
3.13 Fuel mass distribution for optimal CG at a range of fuel loading. 24
3.14 Loading diagram for FV-900. Center of gravity locations corresponding to weight e.g. MTOW and MLW can be read. 29

4.1 Dimensions of the sub-scale model [4] 31
4.2 Wind axis system used in VORLAX and body axis used in experimental model. 33
4.3 Pitching moment derivative as function of moment reference point of the scaled model in VORLAX. CG location of the experimental model indicated by vertical line and experimental C_{m_α} about CG indicated by horizontal line. 34
4.4 Shape formed by the cabin walls containing passengers and cargo. 36
4.5 Moments of inertia of Cappuyns [5] compared to calculated moments of inertia of current FV-1000 at maximum take-off weight. 37
4.6 Moments of inertia of Cappuyns [5] compared to calculated moments of inertia of current FV-1000 at operative empty weight. 37
4.7 Sensitivity matrix. Objective function and constraints are on the x-axis, design variables are on the y-axis. 38

5.1 Overlay of initial and optimized design with stability and control constraints. Topview of FV-900. 40
5.2 Overlay of initial and optimized design with stability and control constraints. Sideview of fins. . 41
5.3 Optimized design of FV family with stability and control constraints. 41
5.4 Overlay of optimized designs with and without stability and control constraints. Topview of FV-900. 42
5.5 Constraints compliance and violation of initial design. Constraint values defined in Equation 3.4 and Equation 3.5. 43

5.6 Constraints compliance and violation of optimized design with stability and control constraints. Constraint values defined in Equation 3.4 and Equation 3.5. 44
5.7 FV-800: Scaled constraints evaluated at a range of CG. Feasible range of CG indicated by red double arrow. 45
5.8 FV-900: Scaled constraints evaluated at a range of CG. Feasible range of CG indicated by red double arrow. 45
5.9 FV-1000: Scaled constraints evaluated at a range of CG. Feasible range of CG indicated by red double arrow. 46
5.10 Loading diagram of the optimized FV-900 loaded as described by Case 1 in Table 5.3. 47
5.11 Loading diagram of the optimized FV-900 loaded as described by Case 2 in Table 5.3. 48

List of Tables

2.1 Design specifications of the Flying-V family. 7
2.2 Control surfaces specifications. 9

3.1 Design variables shown in Figure 3.2. 12
3.2 Constraints separated between stability & control and geometric. 14
3.3 Weight groups in mass distribution model. 18
3.4 Control requirements and critical conditions in which they must be evaluated. 28

4.1 Stability and control derivatives of the sub-scale Flying-V model. Computational and experimental results, $x_{\text{ref}} = 34\ \%\bar{c}$. 33
4.2 Corrections applied to the stability and control derivatives. 34
4.3 Comparison between operative empty weight calculated by simplified and full weight model for different fuselage and outer wing length combinations and all other inputs kept equal. 35
4.4 Inputs to the calculation of the volume between the fuselage walls and results. 36

5.1 Flying-V family optimization results with design variables and fuel mass. 40
5.2 Performance characteristics of the FV family for initial and optimized designs. 40
5.3 Center of gravity of the optimized FV-900 for different loading combinations. In all cases the passengers and cargo are concentrated in the back of their compartments and the fuel is distributed using the system explained in section 3.4. 46

Nomenclature

Latin symbols

A	area	[m^2]
b	wingspan	[m]
c	chord	[m]
C_L	lift coefficient	[-]
C_D	drag coefficient	[-]
C_Y	side force coefficient	[-]
C_m	pitching moment coefficient	[-]
C_l	rolling moment coefficient	[-]
C_n	yawing moment coefficient	[-]
g	gravitational acceleration	[m/s^2]
I	moment of inertia	[kg m^2]
h	height	[m]
L	length	[m]
m	mass	[kg]
n	load factor	[-]
p	roll rate	[rad/s]
q	dynamic pressure	[N/m^2]
q	pitch rate	[rad/s]
R	range	[m]
S	wing area	[m^2]
T	thrust	[N]
V	velocity	[m/s]
V	volume	[m^3]
W	weight	[N]
w	width	[m]

Greek symbols

α	angle of attack	[rad]
β	sideslip angle	[rad]
δ_a	aileron deflection	[rad]
δ_e	elevator deflection	[rad]
δ_r	rudder deflection	[rad]
γ	flight path angle	[rad]
Λ	sweep angle	[rad]
ϕ	bank angle	[rad]

1

Introduction

The Flying-V is a novel aircraft concept for passenger transport which promises a much higher fuel-efficiency than a conventional tube-and-wing aircraft with the same wingspan and payload. There is no fuselage with a separate lifting surface, instead the passenger cabin and cargo containers are integrated into the wing. Thanks to this configuration the aerodynamic drag and the weight are reduced compared to a conventional aircraft designed for the same payload and range.

Since the first studies by Benad at Airbus in 2015 [1], much more research into the flight characteristics has been done and improvements have been made to the design of Flying-V by focusing in more detail on several aspects including structures, aerodynamics, cabin configuration, landing gear, engine-airframe integration, and family concept. The handling qualities of the configuration were investigated by Cappuyns, who revealed rudder control power deficiencies for steady heading sideslip and trim in a coordinated turn [5]. It was demonstrated experimentally by Ruiz Garcia et al. that the aircraft is statically stable around the longitudinal, directional, and lateral axes [6].

Unlike other flying-wing type aircraft like the blended wing body, the cross-section is constant along a certain portion of the length. An advantage of having a constant cross-section is that plugs can be added or removed to obtain multiple versions of the airplane that differ in number of passengers. Having an aircraft family with a high degree of commonality between versions is attractive from a cost-manufacturing perspective. The current Flying-V family consists of three members ranging from 290 to 360 passengers. Recent work on the Flying-V family by Oosterom [3] has shown that a large excursion of center of gravity occurs during loading and unloading of the airplane. Active CG control during flight may reduce trim drag penalties. Also, constraints on lateral and directional control and on control power required to rotate the airplane during take-off have not been included into the optimization. The effects of these stability and control constraints on the performance indicators of the Flying-V need to be investigated.

1.1. Research Objective

In this research the feasibility of a family of Flying-V aircraft in terms of stability and control is investigated. The main objective of this research is *to include stability and control constraints in the optimization for minimum fuel burn of the Flying-V family and proposing a loading/unloading strategy by means of modelling the aerodynamic coefficients, matrix of inertia, and CG excursion.* This objective is accompanied by the following research question:

What is the effect of stability and control constraints on the key performance indicators of the Flying-V family?

The research question is divided into several supporting sub-questions:

1. What is the effect of stability and control constraints on fuel burn performance?
    - How do longitudinal and lateral/directional stability and control derivatives depend on design variables?
    - Which stability or control constraints are driving in the optimization for fuel burn performance?

2. To what extend can active center of gravity control improve fuel burn performance?
    - What is the effect of payload and fuel loading strategy on center of gravity excursion during flight?
    - What is the best center of gravity strategy for maximum trimmed lift-to-drag ratio?

1.2. Thesis Outline

In the coming chapters, the following contents will be presented. First, some background information on flying wings and the Flying-V will be provided. This also includes an explanation of the top-level requirements, parametrization, and multidisciplinary analysis framework. The subsequent chapter contains the discussion of all analysis modules and optimization method. This is logically followed by a chapter on verification and validation of the proposed methods. Finally, the results are presented and supported with conclusions.

2
Background

This chapter provides background information to the Flying-V design, starting with concept of a flying wing, continuing with development of the Flying-V into its current form.

2.1. Flying Wings

The Flying-V is a type of flying wing aircraft. A flying wing is defined as an airplane that consists of one lifting surface without separate fuselage or horizontal tail. It may however include a vertical tail or winglets. The idea of a flying wing configuration has been pursued since the beginning of manned flight in the early twentieth century. John Dunne produced the first practical tailless aircraft between 1907 and 1914 as a swept biplane. Well-known early flying wing developers are the German Horten brothers who developed more than 20 flying wing aircraft in the period between 1931 and 1960 [7], like the Horten Ho 229 shown in Figure 2.1. Examples of existing aircraft currently in production that can be classified as flying wings are the Northrop Grumman B-2 Spirit, a strategic bomber, and the Lockheed Martin RQ-170 Sentinel, a UAV for aerial reconnaissance. A flying wing has several advantages compared to a conventional tube-and-wing aircraft that has been used for commercial airliners since the 1950s and which has mostly reached its limits in terms of fuel efficiency. Bolsunovsky et al. [8] describe the following factors that contribute to an increased lift-to-drag ratio: the larger structural depth allows an increase in wingspan with less weight penalties, the larger wing chord results in higher Reynolds numbers, and the absence of a horizontal stabilizer reduces skin friction and induced drag.

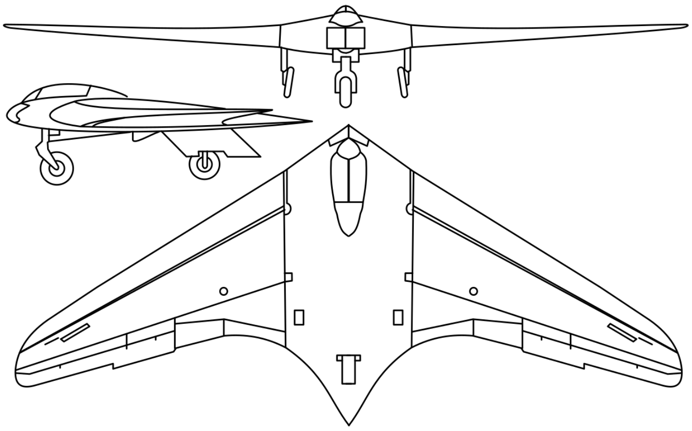

Figure 2.1: Horten Ho 229 prototype fighter.

Despite the potential gain in aerodynamic performance, a flying wing passenger transport aircraft has not been produced yet. After all, the flying wing configuration poses some challenges to overcome mainly related to stability and control that could forestall certification for commercial aviation. It could also be problematic to fit all equipment, payload, and the pilot in the wing.

Directional stability by means of a vertical tail can be difficult to achieve with a flying wing, since a vertical stabilizer would often have a too short moment arm to the aerodynamic center to be effective. A swept flying wing can achieve directional stability using sweep and the aspect ratio that is seen by the incoming airflow. When the aircraft is flying under a sideslip angle, the aspect ratio of one side of the wing is increased, while the aspect ratio of the other side is decreased. The difference in induced drag can generate a restoring yawing moment. This principle has been used by Northrop on the YB-49.

The small moment arm between the aerodynamic center and vertical tail surfaces to which rudders are attached complicates yaw control by means of a rudder in flying wings. Therefore, flying wings often use alternative means of yaw control. These methods usually involve generating differential drag using for example split ailerons/rudders or spoilers. In Figure 2.2, the Northrop Grumman B-2 Spirit is shown with split rudders on the outboard part of the wing.

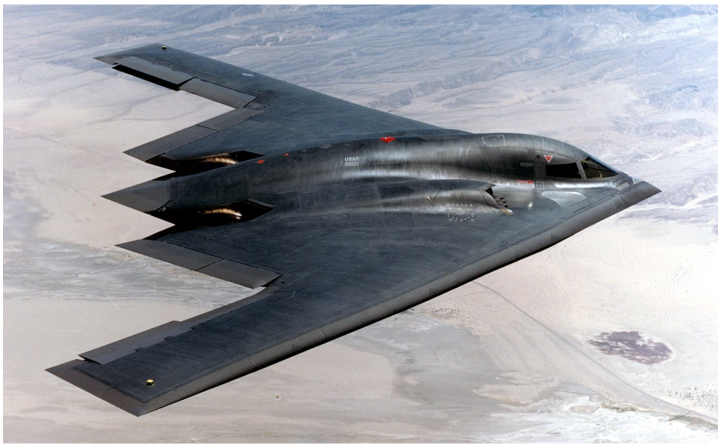

Figure 2.2: B-2 Stealth Bomber employing split rudders for yaw control.

Since flying wings have no horizontal tail and elevator, pitch control is provided by control surfaces on the trailing edge of the wing. These surfaces are similar to the ailerons on a conventional aircraft and can also be used for roll control and are therefore called elevons. A plain flying wing has its aerodynamic center ahead of the center of gravity, making it unstable in pitch. Adding sweep and washout by decreasing incidence angle towards the tip or adding reflex camber to create a downthrust at the tip are ways to achieve longitudinal stability. These modifications are however at the cost of aerodynamic efficiency. Control surfaces for pitch control on flying wings are located closer to the center of gravity than on conventional airplanes. Due to the shorter moment arm the control surfaces must generate larger forces, increasing the drag. The aerodynamic center tends to shift forward at higher angles of attack, potentially creating a pitch-up tendency which is normally countered by the horizontal stabilizer. Thus, it is important to know the location of the aerodynamic center and ensure that it stays behind the center of gravity in the operational range of angles of attack. On the other hand, a too large static margin may cause excessive control authority required for take-of rotation and limit angle of attack and airspeed conditions in which trim can be achieved. Care has to be taken that control surfaces at the trailing edge do not lose effectiveness at high angles of attack due to flow separation.

Another type of tailless aircraft similar to a flying wing, called the Blended Wing Body (BWB), has been considered in several design studies for passenger transport aircraft. It incorporates smooth transition between fuselage and wing. An extensive overview of the development of the BWB is given by Liebeck [9]. It includes the results of a study on the Boeing BWB which has 800 passengers and flies at Mach 0.85 that shows a reduction in take-off weight and fuel burn per seat mile in the order of 15 and 27 percent respectively compared to a conventional baseline. The high aerodynamic efficiency of the BWB is a result of the lower wetted area per unit volume and lower interference drag compared to the tube-and-wing, as explained by Qin et al. [10]. The aerodynamic optimization reported by this paper also led to the conclusion that the ideal lift distribution of the BWB is a combination of a triangular and elliptical lift distribution. In this way, a good balance between lift induced drag wave drag due to shock formation is obtained. This idea was also adopted in later stages of the Flying-V design.

2.2. Development of the Flying-V

The concept of the Flying-V was first studied by Benad in 2015 together with TU Berlin and Airbus. The Flying-V contains two pressurized cabins inside a wing that is swept in the shape of a V, see Figure 2.3. Projecting the circular section in streamwise direction, an elliptical shape is obtained that can be fit into an airfoil. Elevons at the trailing edge provide longitudinal and lateral control and fins including rudders on the wing tips are used for directional stability and control. Due to the relatively large wing area, no high-lift devices are required. It has a shorter length in flight direction than a conventional configuration, which is beneficial for limiting the center of gravity range. Two turbofan engines are placed above the trailing edge. The analysis concluded that this configuration could have a 10 % higher L/D and 2 % lower emtpy weight than the Airbus A350-900 reference aircraft. Other potential benefits include a simple design with less separate parts and engine noise shielding from the ground [1].

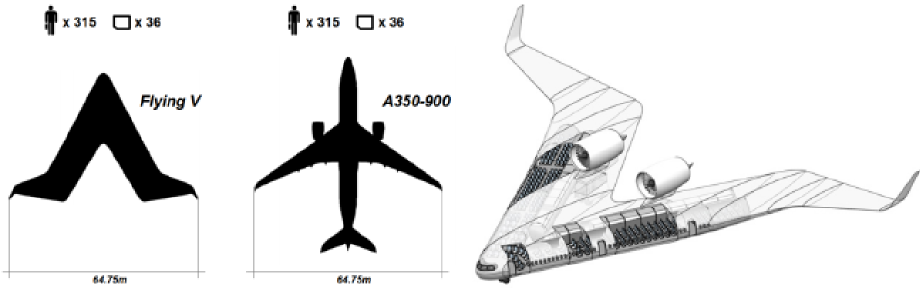

Figure 2.3: Flying-V concept top-view next to Airbus A350-900 including isometric view of the concept [1].

Since then, more work and research has been done on various aspects of the Flying-V which have led to updates to the design. Faggiano [11] continued the aerodynamic design in further detail by performing a shape optimization combined with an aerodynamic solver. A multi-fidelity design space exploration was done, meaning that a lower fidelity vortex lattice tool was used first to rapidly obtain a feasible design space and only the most promising design vectors were analyzed using the higher order Euler method. Results of this optimization are an increase in sweep angle of both the inboard and outboard part of the wing and increased washout. A major design change was to replace the initial pressurized cabin and cargo compartment of circular cross-section by an oval fuselage cross-section. Using an oval cross-section allows more design flexibility, is more volume efficient, the aerodynamic performance can be improved due to lower thickness to chord ratio.

A design and analysis of a Flying-V structure concept has been performed by Van der Schaft [12], where it was shown that the proposed oval fuselage is structurally feasible. The structural feasibility was also proven by Claeys [13], who used several software packages leading to a FEM optimization to obtain structural mass. The engine-airframe integration has been investigated by Rubio Pascual [14] by analyzing the influence of spatial position and orientation of the twin engines using an Euler-based solver and a surrogate model. It was shown that the ideal engine location is slightly above the wing and behind the trailing edge. This gives a minimum perturbation on the lift-to-drag ratio in cruise while obtaining a good compromise between different requirements. The engines were suggested to be placed above the main gear struts to enable a shared structure and limit the influence on mass and CG. Bourget [15] has investigated the effect of implementation of the landing gear according to the criteria of landing gear weight, ground manoeuvre, rotation ability, fairing drag, cabin floor height, and lateral stability derivatives. The landing gear dimensions and position were determined. The flight characteristic of the Flying-V have been investigated in several studies using a scaled model that was tested in a wind tunnel.

Recently, Oosterom [3] investigated fuel-burn performance of a Flying-V aircraft family of three members with a certain level of commonality. A fast method for aerodynamic analysis and weight estimation were developed along with computationally efficient fuel burn performance model. An optimization proved the feasibility of a Flying-V family with the largest two members having a reduction of 20 and 22 % fuel burn compared to the reference conventional aircraft and an acceptable penalty in fuel-burn performance compared to individually optimized aircraft. The results showed that the shift in center of gravity during a mission is relatively large.

2.3. Stability and Control Considerations of the Flying-V

The stability and control constraints are often critical in low speed and high angle of attack conditions, with the center of gravity at either the most forward or most aft location. The flight characteristics of the Flying-V in approach speed and high angle of attack have already been studied using wind tunnel tests on a sub-scale model. Flow visualizations have shown that after a certain angle of attack, leading edge vortices appear on the wing surface [2]. The vortex formation has the effect of increasing the lift coefficient due to vortex lift and delaying stall to high angles of attack. Similar effects also occur in other highly swept configurations like the delta wing. The maximum lift coefficient as found by Viet was 1.08 at an angle of attack of 42 degrees. It can be said that the maximum lift coefficient is lower compared to conventional aircraft and the stall angle of attack is higher. The lift slope at low angles of attack was around 1.9 per radian and increased to a maximum of 2.4 per radian at around 13 degrees angle of attack due to vortex effects.

The wind tunnel measurements have shown that the pitching moments stability derivative C_{m_α} is negative indicating static longitudinal stability until 20 degrees angle of attack after which pitch break occurs and the slope of pitching moment coefficient becomes positive. At this angle of attack, several smaller vortices combine into one primary vortex which cause the movement of center of pressure to change direction from afterward to forward. It was also shown that the location of the neutral point is relatively constant until the pitch break occurs. For low-speed conditions, it should be possible to trim the aircraft at large angles of attack, while keeping sufficient control authority for pitch control. In cruise conditions, the control surface deflection for trim should be small to minimize drag. The curve of pitching moment coefficient versus angle of attack shifts up or down with elevon deflection. Plotting lines for multiple deflection angles shows the range of angles of attack for which a moment coefficient of zero can be achieved required to trim the aircraft. An example of this is shown in Figure 2.4. Here the pitch break behaviour at around 20 degrees angle of attack can be clearly seen.

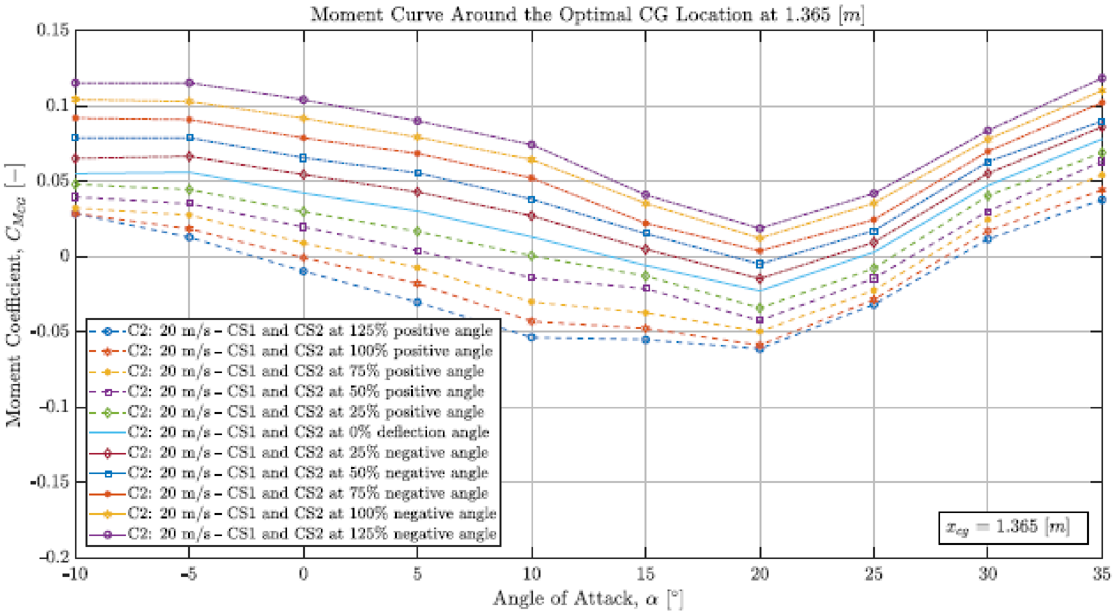

Figure 2.4: Curve of moment coefficient around the center of gravity of the scaled Flying-V model for a range of elevon deflections [2]. CS1 and CS2 refer to the inboard and outboard elevons respectively.

The deflection of control surfaces for trim can be positive (trailing edge down) or negative (trailing edge up) depending on the angle of attack, since the center of pressure shifts with angle of attack. When the center of pressure is in front of the center of gravity, the lift contribution of the elevon should be positive to generate a nose-down moment and when the center of pressure is behind the center of gravity, the lift contribution should be negative to generate a nose-up moment. For the optimal CG as suggested by Viet, this shift occurs at around 11 degrees angle of attack. The impact of control surface deflection on the lift coefficient is however relatively small, as pointed out by Palermo [16]. The approach used by Palermo to determine the optimal center of gravity location was maximize the maximum trimmed lift coefficient while enabling trim at the entire range of encountered angles of attack. This leads to a center of gravity of 1.336 m behind the nose. This allows the aircraft to be trimmed just until the maximum stable angle of attack of 20 degrees.

The handling qualities of the Flying-V have been studied by Cappuyns [5] on the basis of criteria selected from the the Military Handbook MIL-HDBK-1797 and EASA's CS-25. Here the flight dynamics were analyzed using a specialized toolbox. The longitudinal and directional/lateral stability modes were tested. The Flying-V was shown to meet all requirements on the damping and frequency of the phugoid and short period eigenmotions. The Dutch roll mode was found to be unstable, while the spiral modes meet the requirements for acceptable flight qualities.

The coefficient C_{n_β} was found to be positive for all tested conditions, indicating directional stability. A sideslip disturbance tends to be decreased by a positive yawing moment. The absence of a destabilizing fuselage in the Flying-V is beneficial for directional stability. The dihedral effect C_{l_β} is mainly affected by the wing dihedral and wing sweep, which both aid lateral stability. It should have a negative value for stability. When this is the case, the bank angle that causes the aircraft to sideslip is reduced by a rolling moment in the opposite direction. This restoring rolling moment is caused by the increase in lift on the side of the incoming sideslip component of the free-stream velocity, which is the lower wing. The increase in lift on this side is generated by the increased angle of attack due to the dihedral angle.

It was observed by Cappuyns that decreasing the dihedral angle and increasing the winglet length improved the Dutch roll behaviour as demonstrated by the longer time to double. The decreased dihedral angle decreases the magnitude of C_{l_β} without losing static lateral stability, while the increased winglet length increases directional stability. This combination of properties is indeed known to be beneficial for better Dutch roll stability. Several control maneuvers were limited by insufficient rudder control power in one engine inoperative condition and low speed: steady heading sideslip, trim in coordinated turn, and bank-to-bank.

2.4. Current Design

As seen in the previous sections, the design is not started from scratch. The top-level requirements for the Flying-V family have already been determined. A variable geometric model of the Flying-V is available along with several analysis modules.

2.4.1. Top-level Requirements

The Flying-V family consists of three variants that can be deployed for different design missions. The design mission is defined in terms of payload and range. The payload consists of the passenger and cargo weight. The design payload is the weight of the maximum number of passengers. The cabin must have enough space to fit all passengers. Additionally, the cargo compartment must be large enough to fit the required cargo at maximum structural payload. The airplane cruises at Mach 0.85 and an altitude of 11 km. The Flying-V must satisfy the same airport requirements as the Airbus A350 family. This puts constraints on the maximum span, tail height, and approach speed. The design specifications are shown in Table 2.1.

	Unit	FV-800	FV-900	FV-1000
Number of passengers	-	293	328	361
Design range	km	11160	14800	15350
Design payload	10^3 kg	27.6	30.9	34.0
Maximum structural payload	10^3 kg	35.7	53.8	67.1
Approach speed	m/s	72	72	76

Table 2.1: Design specifications of the Flying-V family.

2.4.2. Geometric Model and Parametrization

The parametrization of the geometry of the Flying-V used in this research has been made by Hillen [17]. The planform is described by the chord lengths at several sections, sweep angles of the inboard and outboard wing, and lengths of the segments. The different segments are the untapered part of the cabin, the tapered part of the cabin, the part between the inner and outer wing, and the outer wing, see Figure 2.5. The cross-section of the outer wing sections is described by CST coefficients. The cross-section of the inboard wing sections is described by using width and height of the cabin, keel height and crown height, chord length, and trailing edge position as shown in Figure 2.6. The dihedral and twist angles of the inboard and outboard wings are also adjustable. The parametrization of the fins is provided by Horwitz [18], and consists of bend radius, cant angle, sweep angle, length, tip twist, and taper ratio.

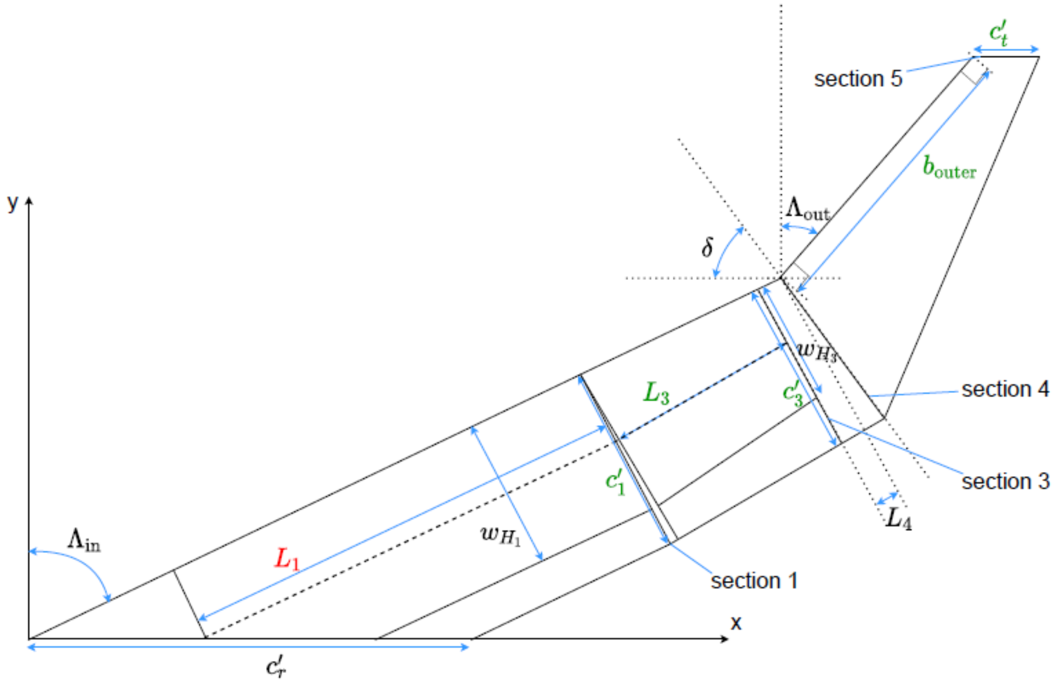
c'_t
section 5
b_{outer}
y
Λ_{out}
δ
w_{H_3}
L_3
c'_3
section 4
section 3
c'_1
L_4
Λ_{in}
w_{H_1}
L_1
section 1
x
c'_r

Figure 2.5: Planform parametrization.

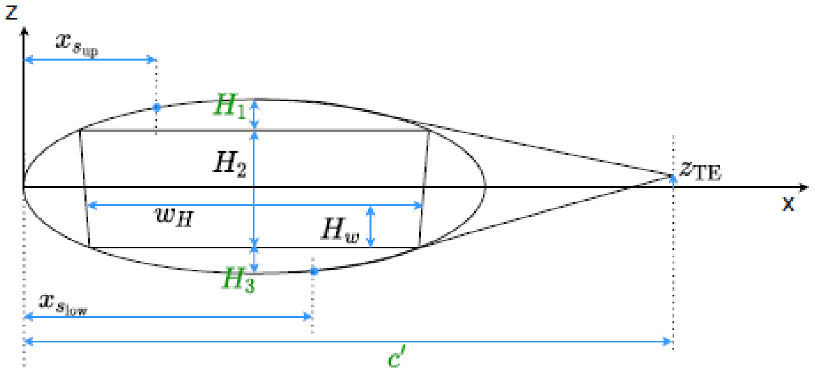
z
$x_{s_{\text{up}}}$
H_1
H_2
z_{TE}
x
w_H
H_w
H_3
$x_{s_{\text{low}}}$
c'

Figure 2.6: Cross-section parametrization.

2.4.3. Control Surfaces

The Flying-V is maneuvered using two types of control surfaces shown in Figure 2.7. Pitch and roll rotation is achieved using elevons which are located on the trailing edge of the outer wing. Yaw rotation is achieved by moving the rudders which are attached to the fins. In this report, an elevon deflection used for pitch control is called elevator deflection δ_e and an elevon deflection used for roll control is referred to as aileron deflection δ_a. The elevon of one wing-half can be split into multiple surfaces as was done in previous research, but in this work the elevon is one surface that spans over almost the entire trailing edge of the outer wing. The dimensions of the control surfaces and directions of positive deflection are shown in Table 2.2.

Control surface	Inboard length [m]	Outboard length [m]	Positive deflection
Rudder	$0.4c_{\mathrm{r_{fin}}}$	$0.4c_{\mathrm{t_{fin}}}$	Trailing edge pointing starboard
Elevon	1.56	0.66	Pitch: both sides down Roll: starboard up, port down

Table 2.2: Control surfaces specifications.

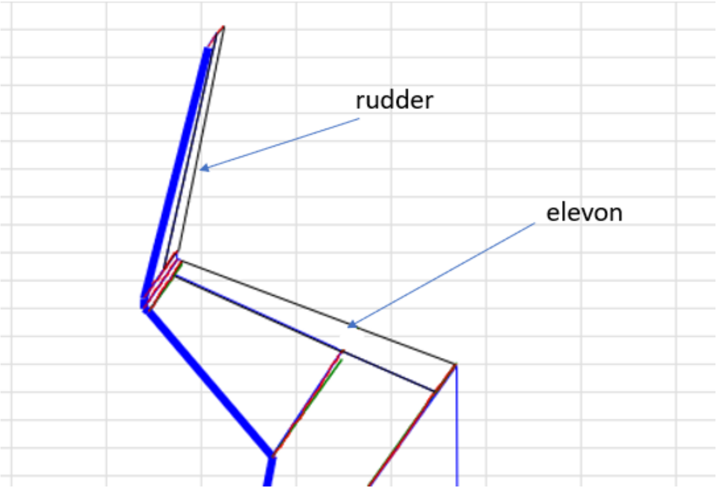

Figure 2.7: Control surfaces on one side of the wing.

2.4.4. Internal Layout

The floor plan of the FV-900 proposed by Oosterom and Vos is shown in Figure 2.8. It shows the locations of the seats, lavatories, galleys, closets, doors, cargo containers, and fuel tanks. The engines and landing gear are attached to the same part of the wing for structural efficiency. Fuselage plugs are added or removed behind and in front of this part to obtain the larger and smaller family versions. The plugs contain passenger seats but no emergency exits and lavatories. The cargo containers are located in the cargo hold behind the passenger cabin and the cargo hold is separated from the passenger cabin by a wall. The fuel tanks are located along the trailing edge of the inboard wing and between the front and aft spars of the outboard wing. The trailing edge fuel tanks is split into two parts to make room for the engine and landing gear. Thus, there are three fuel tanks in each wing-half.

2.5. ParaPy Framework

The geometric model and analysis modules are created using ParaPy, a Python library for Knowledge Based Engineering (KBE). KBE is a technology that aims to reduce development time by automating the design process [19]. It uses demand-driven evaluation, which means that only the required values are computed, saving computational resources. In ParaPy, the geometric input variables are used to generate a CAD model. Object-oriented programming is useful for family design. The class defining the full aircraft can be reused as objects with different inputs to generate the different family variants. Several simulation tools are available and any tool programmed in Python can be added. When an input variable is changed, the CAD model is automatically updated, as are the results of the analysis modules. This is important since the inputs will be varied many times during the optimization. The analysis modules created for this research will be added to the ParaPy framework.

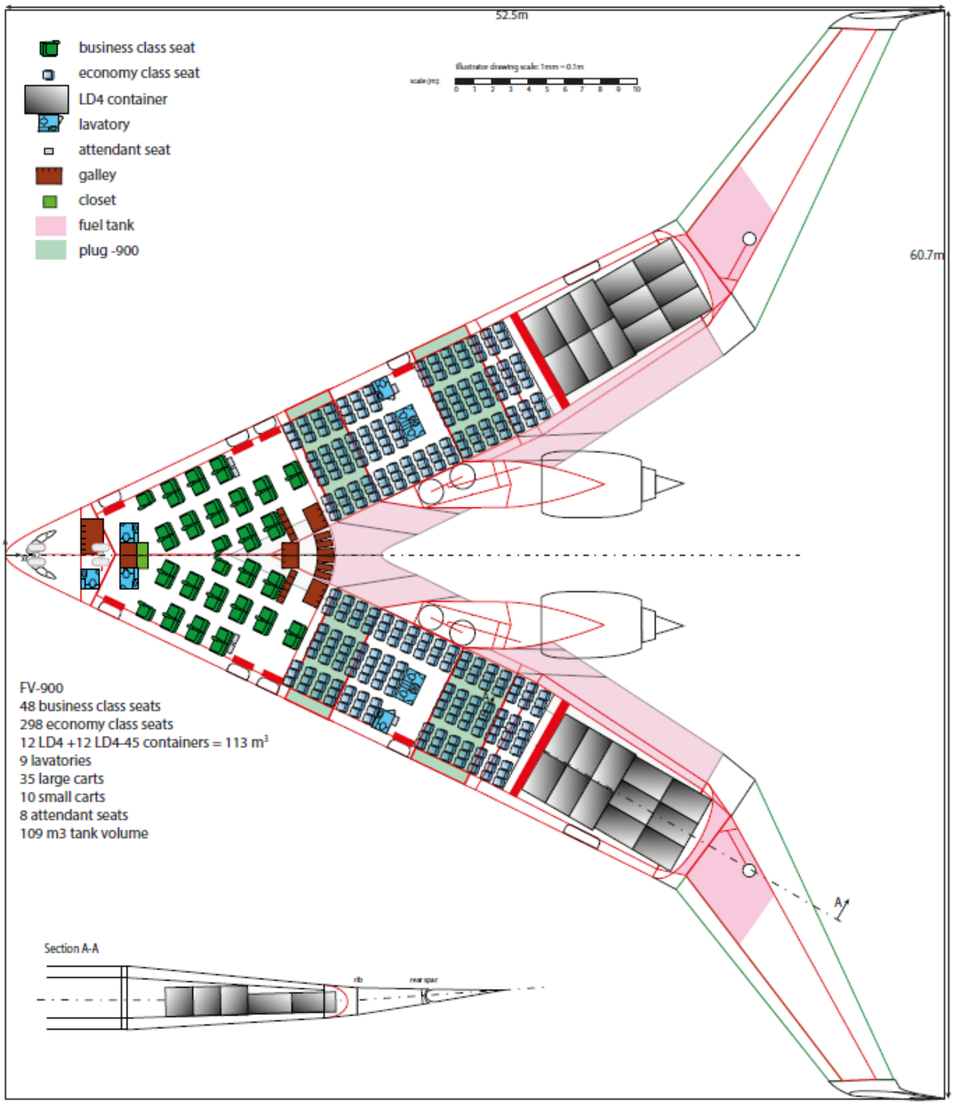
52.5m
60.7m
business class seat
economy class seat
LD4 container
lavatory
attendant seat
galley
closet
fuel tank
plug -900
illustrator drawing scale: 1mm = 0.1m
scale (m):
0
1
2
3
4
5
6
7
8
9
10
FV-900
48 business class seats
298 economy class seats
12 LD4 +12 LD4-45 containers = 113 m^3
9 lavatories
35 large carts
10 small carts
8 attendant seats
109 m3 tank volume
A
Section A-A
rib
rear spar

Figure 2.8: Floor plan layout of the FV-900. [3]

3

Methodology

In order to answer the research question, several analysis modules are required. The models used for aerodynamics, mass and center of gravity, fuel burn performance, and stability and control are discussed in this chapter. Beforehand, it is explained how the disciplines are linked together for optimization.

3.1. Multidisciplinary Design Optimization

Analysis modules have been created for weight estimation, aerodynamic analysis, fuel burn analysis, mass distribution, and stability and control. The results of the analyses are used to determine the fuel burn performance and check compliance with stability and control requirements. The flow of inputs and outputs between the analysis modules is presented in Figure 3.1. This figure shows the Extended Design Structure Matrix (XDSM). The green blocks are the analysis modules and the grey blocks are inputs and outputs. The blocks above and below the analysis modules are inputs to that module and the blocks on the same horizontal position are outputs. For example, the operative empty weight W_{OE} is an output of the weight estimation and an input to the aerodynamic analysis. The top row of the matrix contains the vector of design variables $\bar{x}$. In this case these are geometric parameters that describe the shape of the aircraft. They are inputs to most of the analysis modules. There are more inputs to the analysis modules than just the design variables, but they are not shown in the diagram because they are constant parameters like payload weight, cruise speed, and engine specific fuel consumption. The red blocks on the diagonal are the constraints and objective function. Their outputs are fed to the optimizer which tries to choose a new design vector that is closer to the optimum while satisfying the constraints. Some analysis modules require a guess value of their output as an input. For example the maximum take-off weight is used as input to calculate the fuel weight, but the maximum take-off weight itself also depends on the fuel weight. Furthermore, the lift-to-drag ratio in cruise depends on fuel weight, while the lift-to-drag ratio is needed to calculate fuel weight. Thus, a convergence loop is necessary to obtain consistent values for input and output fuel weight. This is done by the MDA (Multidisciplinary Analysis Coordinator) block shown in yellow.

3.1.1. Design Variables

Most planform variables are taken as design variables, since they are expected to have most effect on stability and control behaviour compared to cross-section variables. All design variables are shown in Figure 3.2 and listed in Table 3.1. The sweep of the inboard wing is kept constant, since the current sweep angle was determined using higher order aerodynamic analysis by Faggiano to result in relatively low wave drag and wave drag cannot be predicted with the current methods. The chord lengths are kept constant, since it was found that they could not change too much while keeping valid geometry without changing sectional variables which would result in having too many design variables to have acceptably short computational time. As explained by Oosterom [3], the three family members must have as much common parts as possible, since this is attractive from a manufacturing-cost perspective. To have a high degree of commonality, the variables will be the same for all family members, except the length L_1 of the part of the cabin that has a constant cross-section, see Figure 3.2.

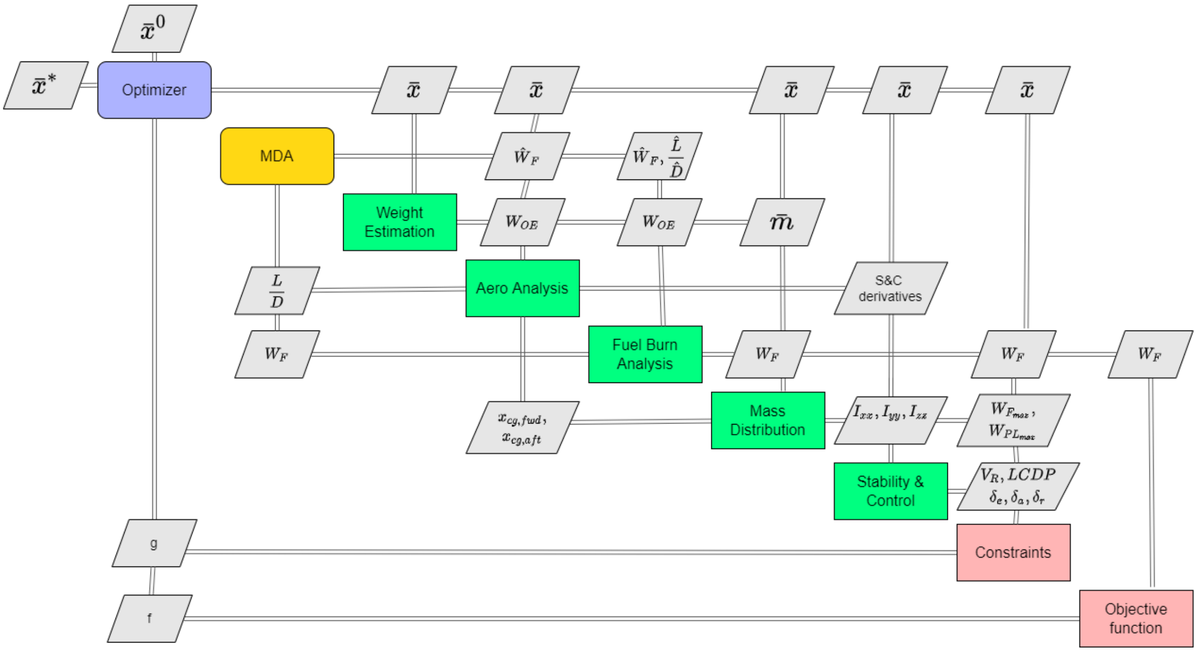
$\bar{x}^0$
$\bar{x}^*$
Optimizer
$\bar{x}$
$\bar{x}$
$\bar{x}$
$\bar{x}$
$\bar{x}$
MDA
$\hat{W}_F$
$\hat{W}_F, \frac{\hat{L}}{\hat{D}}$
Weight Estimation
W_{OE}
W_{OE}
$\bar{m}$
$\frac{L}{D}$
Aero Analysis
S&C derivatives
W_F
Fuel Burn Analysis
W_F
W_F
W_F
$x_{cg,fwd}$, $x_{cg,aft}$
Mass Distribution
I_{xx}, I_{yy}, I_{zz}
$W_{F_{max}}$, $W_{PL_{max}}$
Stability & Control
$V_R, LCDP$ $\delta_e, \delta_a, \delta_r$
g
Constraints
f
Objective function

Figure 3.1: Optimization Architecture. All quantities in the grey blocks consist of three values: one for each aircraft family member.

Description	Variable	Unit
Outer wing span	b_{outer}	m
Tapered fuselage length	L_3	m
Fin length	L_{fin}	m
Outer wing sweep	Λ_{out}	°
Untapered fuselage length FV-800	$L1_{800}$	m
Untapered fuselage length FV-900	$L1_{900}$	m
Untapered fuselage length FV-1000	$L1_{1000}$	m

Table 3.1: Design variables shown in Figure 3.2.

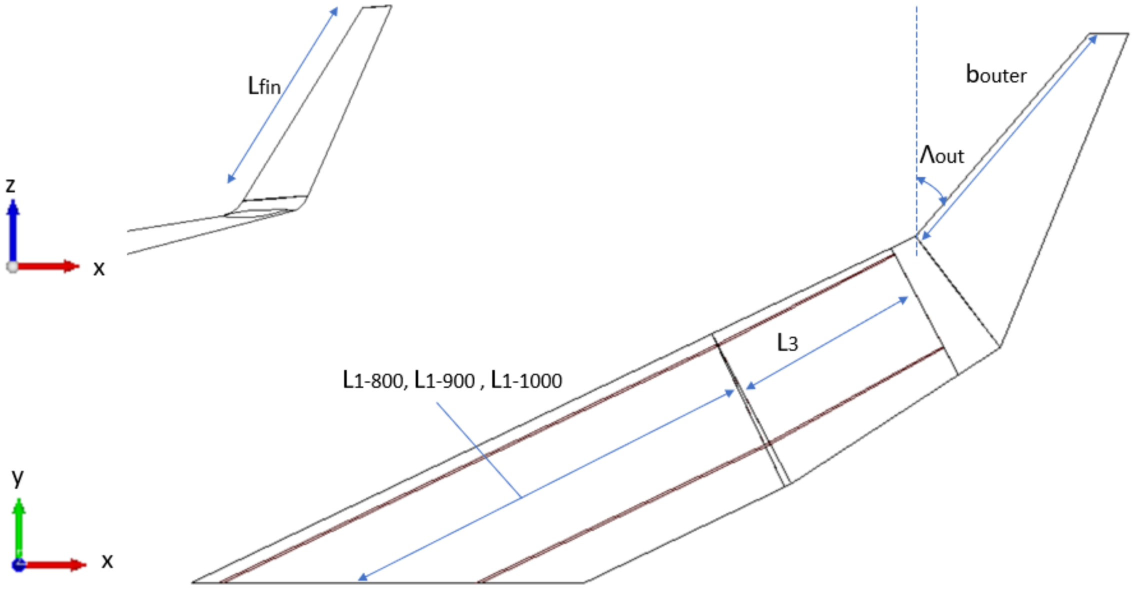
Lfin
z
x
bouter
Λout
L3
L1-800, L1-900 , L1-1000
y
x

Figure 3.2: Design variables.

3.1.2. Objective Function

The objective function is the quantity that needs to be minimized. In this case, the objective function is the average fuel weight of the three aircraft.

$$W_{\mathrm{F}_{\mathrm{avg}}} = \frac{W_{\mathrm{F}_{800}} + W_{\mathrm{F}_{900}} + W_{\mathrm{F}_{1000}}}{3} \tag{3.1}$$

The mathematical statement for the optimization is the following:

$$\text{minimize} : f(\bar{x}) = \frac{W_{\mathrm{F}_{\mathrm{avg}}}}{W_{\mathrm{F}_{\mathrm{avg},0}}} \tag{3.2}$$

$$\text{subject to} : g_i(\bar{x}) \geq 0 \tag{3.3}$$

Where g_i are the values of the inequality constraints and $\bar{x}$ is the vector of design variables.

3.1.3. Constraints

The design must satisfy a number of constraints. The constraints can be divided into two types: stability & control constraints and geometric constraints. The control constraints are explained in section 3.6. Additionally there are three stability constraints which are simply the stability derivatives for longitudinal, lateral, and directional stability evaluated at the most aft center of gravity. They need to have the correct sign to ensure stability. There are also four geometric constraints. The maximum total span is 65 m and maximum tail height is 20.1 m. The design fuel weight must fit inside the fuel tanks of which the volume is calculated by the geometric model. The fuel volume is calculated using the design fuel mass and fuel density of 804 kg/m^3. The volume of the cargo compartment must be larger than the maximum harmonic cargo volume. Since the cargo compartment volume is calculated by subtracting the required passenger cabin volume from the total volume of the trapezoidal part of the fuselage, no extra constraint is needed for the passenger capacity. The calculation of passenger and cargo space is explained in more detail in subsection 3.3.4. The list of constraints is shown in Table 3.2. The constraints are evaluated for the three family versions, making the total number of constraints equal to 63. The constraints are normalized and written as inequality constraints larger than zero in the following manner:

$$c_i \leq c_{i_{\max}} \rightarrow g_i = -\frac{c_i}{c_{i_{\max}}} + 1 \geq 0 \tag{3.4}$$

$$c_i \geq c_{i_{\min}} \rightarrow g_i = \frac{c_i}{c_{i_{\min}}} - 1 \geq 0 \tag{3.5}$$

3.1.4. Search Algorithm

The optimize.minimize function from Python's SciPy library is used for the minimization problem. It takes the initial design variables, objective function and inequality constraints function as input. There are several search algorithms available. The search algorithm must be able to handle constraints and be reasonably fast. Based on these requirements the COBYLA algorithm was selected. It calculates linear approximations to the objective function and constraints to find the gradient information. It behaves like a sequential trust-region algorithm which means that at every iteration there is a radius around the design vector in which the variables can change and this radius decreases at each iteration. The radius of the initial trust-region is set at 20 % of the initial design variables. The algorithm stops when the search radius has reached the minimum value. This value is set to 0.1 %.

Number	Description	Constraint
1	Longitudinal trim: α	$\alpha < 19°$
2	Longitudinal trim: δ_e	$\delta_e < 25°$
3	Pull-up: α	$\Delta\alpha < 10°$
4	Pull-up: δ_e	$\Delta\delta_e < 25°$
5	Steady sideslip: δ_r	$\delta_r < 25°$
6	Steady sideslip: δ_a	$\delta_a < 25°$
7	Steady sideslip: ϕ	$\phi < 5$
8	Engine-out trim: δ_r	$\delta_r < 25°$
9	Engine-out trim: δ_a	$\delta_a < 25°$
10	Engine-out trim: ϕ	$\phi < 5°$
11	Time to bank	$\phi > 60°$
12	Take-off rotation	$V_\mathrm{R} < V_{2_\mathrm{min}}$ - 5 m/s
13	Departure: Dynamic C_{n_β}	$C_{n_{\beta_\mathrm{DYN}}} > 0$
14	Departure: LCDP	LCDP > 0
15	Longitudinal stability	$C_{m_\alpha} > 0$
16	Lateral stability	$C_{l_\beta} < 0$
17	Directional stability	$C_{n_\beta} > 0$
18	Maximum span	$b < 65$ m
19	Cargo and passenger capacity	$V_\mathrm{cargo,hold} > V_{\mathrm{cargo}_\mathrm{harmonic}}$
20	Fuel capacity	$V_\mathrm{tanks} > V_{\mathrm{F}_\mathrm{design}}$
21	Tail height	$h_\mathrm{tail} < 20.1$ m

Table 3.2: Constraints separated between stability & control and geometric.

3.2. Aerodynamic Modelling

Analysis of the performance and flight dynamic behaviour of the Flying-V requires knowledge of the forces and moments acting on it. The aerodynamic forces are generated by pressure differences caused by movement of the air around the vehicle. On the most fundamental level, the motion of fluids is described by the equations for conservation of mass, momentum (Navier-Stokes equations), and energy, of which the derivation is given in many textbooks [20, 21]. These partial differential equations are highly nonlinear and no exact analytical solutions exist. Approximate solutions for the flow-field variables like pressure and velocity can be obtained by making simplifying assumptions and discretizing the equations on a grid. Simplifying the equations reduces the computational cost, but also leads to less accurate results. Higher order methods like RANS and Euler equations theoretically give the most accurate results, but are too computationally expensive to be used in this optimization study. Instead, focus been placed on faster potential flow methods. Potential flow methods are derived under the assumption of inviscid and irrotational flow. The body of interest is modeled as a combination of elementary flow singularities and by applying specific boundary conditions a system of equations is obtained that can be solved for pressure, velocity, or vorticity.

3.2.1. VORLAX: A Vortex Lattice Solver

A commonly used potential flow method for fast analysis and design of aircraft configurations is the vortex lattice method. *VORLAX* is a vortex lattice solver developed by Lockheed-California Company in the 1970's by Miranda et al. [22]. The program has the capability to calculate the aerodynamic load distribution, force coefficients, and moment coefficients on arbitrary wing configurations for subsonic and supersonic Mach numbers. The wing is modeled as a cambered surface of zero thickness. The basic equations used are those describing small-perturbation, linearized, compressible fluid flow. The lifting surfaces are divided into a grid of panels on which horse-shoe vortices are placed. The skewed-horseshoe vortex is the fundamental buiding block and consists of a transverse vortex filament of constant sweep and two trailing legs, see Figure 3.3. The velocity field induced by this horseshoe vortex is obtained by combining the contributions of the three segments. The boundary condition of zero mass flux through the surface is applied at the control points. A system of equations is set up that relates the vortex strengths to the corresponding boundary conditions, which is solved to obtain the pressure coefficient distribution from which the total aerodynamic force and moment coefficients are derived.

The latest revised version of *VORLAX* has been developed in 2020 by Souders and Takahashi [23]. Numerous improvements and bug fixes to the original FORTRAN code have been made, such as drag integration under certain gridding options and revised memory management. It was shown that *VORLAX* can provide remarkably accurate results in a small amount of time on a standard computer. *VORLAX2020* is operated by standard text files. The user can generate input files that include flight conditions and the geometry definition. The input flight conditions are angle of attack, sideslip, Mach number, and pitch, roll, and yaw rates. The output file contains the aerodynamic results. The input and output files files can be easily created and parsed using common coding platforms, like Python in this case. The most important aerodynamic results for this research are the total force coefficients C_L, C_D, C_Y and moment coefficients C_m, C_l, C_n. The coefficients are calculated based on the input wing reference area, mean aerodynamic chord, and moment reference point. The stability and control derivatives are computed by running the solver at different angles of attack, sideslip, angles, and control surface deflections and taking finite differences.

The geometry is represented by a number of optionally cambered thin quadrilateral surfaces. They are parametrized by x,y,z-coordinates of the leading edges, chords, and inclination angles of the inboard and outboard edges of the surfaces. The number of chordwise and spanwise vortices can be selected to control the grid size. The *VORLAX* geometry of the Flying-V is shown in Figure 3.4 and Figure 3.5. The wing consists of multiple surfaces with different leading edge or trailing edge sweep. The fin is placed at a large angle with respect to the plane of the outer wing and its root chord is the same as the tip chord of the outer wing. To get a smoother transition between the main wing and fins, two small surfaces are placed between the outer wing and winglet, increasing the angle with respect to the outer wing plane in steps. Control surfaces like ailerons and rudders are defined as separate surfaces behind the main wing surfaces. To simulate control surface deflection, the inclination angle of the panel representing the control surface can be varied.

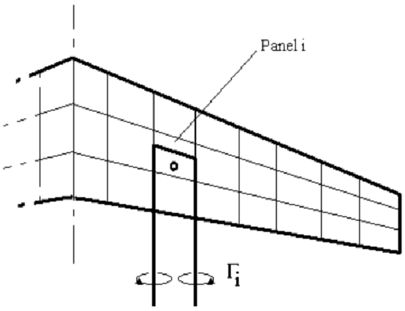

Figure 3.3: Example of panel distribution for vortex lattice method. Horseshoe vortex is shown for one panel. [1]

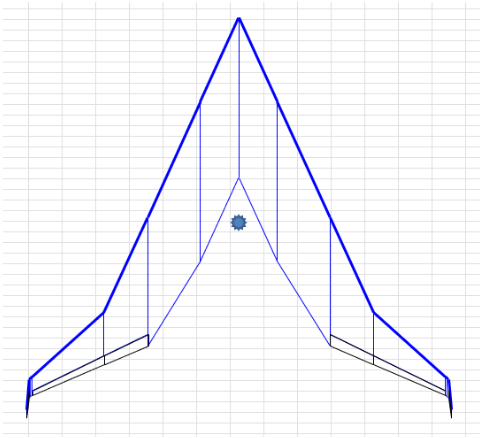

Figure 3.4: VORLAX Representation of a Flying-V planform.

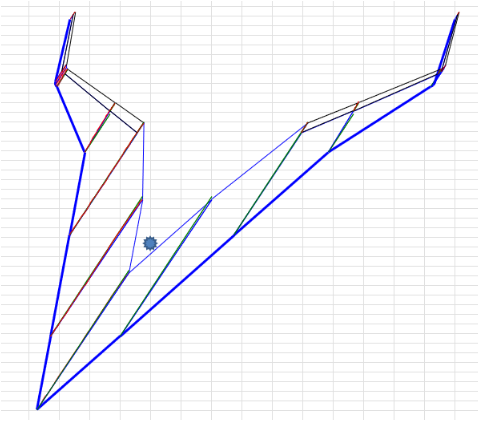

Figure 3.5: VORLAX Representation of a Flying-V isometric view.

---

[1] Source: `http://www.aerodynamics4students.com/subsonic-aerofoil-and-wing-theory/3d-vortex-lattice-method.php`

3.2.2. Viscous Drag Estimation

In order to predict fuel burn performance the total lift-to-drag ratio is required. The part of the drag due to viscous effects is the parasite drag, nondimensionalized as the zero-lift drag coefficient C_{D_0}. However, parasite drag is not calculated by the vortex lattice solver, only the inviscid lift induced drag. Viscous drag is approximated using the viscous module used by Faggiano [11]. Here the airplane is divided into the components wing, nacelles, and pylons and Equation 3.6 is applied to the components.

$$C_{D_0} = C_F \cdot FF \cdot \frac{S_{\text{wet}}}{S} \tag{3.6}$$

The the skin friction coefficient for turbulent flow C_F and form factors FF of the different components are estimated using the empirical relations from Raymer [24] and Torenbeek [25]. However, the parasite drag of the fins has not yet been included. In this research, the size of the fin is a design variable, so its effect on the total drag is relevant. The viscous module was therefore modified to include the viscous drag contribution of the fins. This was done by first calculating the equivalent skin friction coefficient of the wing by dividing the parasite drag contribution of the wing by the ratio of wetted area:

$$C_{F_e} = C_{D_{0,\text{wing}}} \frac{S}{S_{\text{wet}}} \tag{3.7}$$

It is assumed that the fins increase the wetted area by four times the fin area and the wing reference area remains the same. The combined viscous drag coefficient of the wing and fins is then:

$$C_{D_{0,\text{wing+fin}}} = C_{F_e} \frac{S_{\text{wet,wing}} + 4S_{\text{fin}}}{S} \tag{3.8}$$

The pylon drag of Bourget of 3 drag counts is used [15]. The total zero-lift drag coefficient is the sum of the contributions of the wing, fins, pylons, and nacelles:

$$C_{D_0} = C_{D_{0,\text{wing+fin}}} + C_{D_{0,\text{pylon}}} + C_{D_{0,\text{nacelle}}} \tag{3.9}$$

The total drag coefficient is the sum of the inviscid drag coefficient predicted by *VORLAX* and the estimated zero-lift drag coefficient:

$$C_D = C_{D_0} + C_{D_{\text{inv}}} \tag{3.10}$$

3.3. Mass Distribution Estimation

In order to determine the center of gravity and moments of inertia of the aircraft, the mass distribution needs to be known. A mass distribution model has been created using the 3D model of the wing and cabin in the ParaPy framework. Here the wing and cabin are divided into smaller solids and point masses. The smaller solids are obtained by performing automated CAD operations in ParaPy. Every mass is assigned to a three-dimensional solid or point mass. Assuming a uniform distribution of mass per component, the center of gravity of each weight group is equal to the volume centroid of the corresponding solid. The center of gravity and matrix of inertia of the individual solids are calculated by ParaPy. The total center of gravity and moments of inertia can be calculated using Equation 3.11 through Equation 3.14.

$$\bar{x}_{cg} = \frac{\sum_{i=1}^{n} \bar{x}_i m_i}{\sum_{i=1}^{n} m_i} \tag{3.11}$$

$$I_{xx} = \sum_{i=1}^{n} I_{xx_i} + m_i(\tilde{y}_i^2 + \tilde{z}_i^2) \tag{3.12}$$

$$I_{yy} = \sum_{i=1}^{n} I_{yy_i} + m_i(\tilde{x}_i^2 + \tilde{z}_i^2) \tag{3.13}$$

$$I_{zz} = \sum_{i=1}^{n} I_{zz_i} + m_i(\tilde{x}_i^2 + \tilde{y}_i^2) \tag{3.14}$$

3.3.1. Weight Estimation

The masses of the various components need to be estimated to generate a mas distribution. The maximum take-off weight consists of the operative empty weight, payload weight, and fuel weight.

$$W_{\mathrm{MTO}} = W_{\mathrm{OE}} + W_{\mathrm{PL}} + W_{\mathrm{F}} \tag{3.15}$$

The payload weight is fixed for the three family versions. The fuel weight is calculated using the method explained in section 3.5. The operative empty weight, which includes the structure, landing gear, propulsion, operative items, furniture, and systems, is estimated using the Flying-V weight estimation tool created by Oosterom [3]. For this tool, a combination of different methods was used for the structural weight of the different parts of the aircraft. The weight of the part containing the oval fuselage structure is calculated using a semi-analytical oval fuselage weight estimation method that was developed by Schmidt et al [26]. The fuselage structural weight is calculated at 30 sections based on the loads. The outboard part of the wing, which is more similar to a conventional wing structure is calculated by a quasi-analytical tool called EMWET developed by Elham [27]. The non-structural and payload weights are estimated by empirical relations from the Torenbeek method [25].

This weight model has been simplified for the current research to reduce computation time. Before, the structural weight of the fuselage and outer wing were calculated by sizing the structural members using the lift distribution in several load cases. Iterations between the aerodynamic solver and structural analysis tools were required. Now, the full calculation is only done for the initial design. Using the masses and volumes of the shapes, densities of the shapes are calculated. These densities are kept constant for the shapes. The shapes in question are the 30 fuselage sections and the outer wing solid. When the input dimensions are changed, the new structural weights are calculated by multiplying the densities with the new volumes. The operative empty weight now only depends on the geometric inputs. The other masses besides fuselage and outer wing structural mass are still calculated by the original tool.

3.3.2. Weight groups

The weight groups that the aircraft consists of are presented in Table 3.3. The location of the fuel tanks, passengers and cargo are shown in Figure 3.6. The fuselage weight is divided over 30 sections. The oval fuselage solid is divided into the same number of parts and the masses of these individual sections are assigned to these solids as shown in Figure 3.7. The locations of the point masses and solids modelling the remaining weight groups are shown in Figure 3.8.

The passengers and cargo weight is assumed to be distributed in the trapezoidal part of the fuselage, with the passenger cabin in front of the cargo compartment. There are three fuel tanks in each wing half. The two tanks closest two the nose take up the space in the trailing edge behind the aft wall of the trapezoidal structure supporting the oval fuselage. The whole trailing edge cannot be occupied by the fuel tanks. The space between the two fuel tanks is reserved for the engine and landing gear. A part in front of the most forward tank is occupied by cabin equipment. The outer tank is inside the outer wing between the front and aft spars which are located between 15 and 60 percent of the chord drawn perpendicular to the leading edge. The end of the fuel tank is at 30 percent of the span of the outer wing. A scaling factor of 0.9 is applied to the fuel volumes to reserve space in the tanks for systems like pumps, valves and pipes and structural parts.

The mass of the flight control system is assumed to be distributed in the outer wing, where the control surfaces are located. The hydraulic and electrical systems mass is spread throughout the wing. The instruments are located near the nose as a point mass. The PACKS (pressurization air conditioning kits) and APU (auxiliary power unit) are relatively heavy components and their masses are taken as point masses placed in the middle of the fuselage. The furnishing weight consists of flight deck furnishing, passenger seats, galleys, lavatories, floor, sound proofing, cargo handling, ogygen, fire provisions, and escape provisions. The operating items consist of crew provisions, passenger supplies, pot water, and emergency equipment. The mass of the furnishing and operating items is modeled to be evenly distributed inside the oval part of the fuselage. The structural mass of the outer wing is distributed evenly in the outer wing volume. The fuselage trailing edge is mass is the structural mass of the inner wing that is not part of the oval fuselage structure. The solid representing this mass is obtained by taking the inboard wing and removing the oval cabin part. The nose weight group includes the front bulkhead, windscreen, and miscellaneous doors and is modeled by a point mass at the start of the cabin, while the aft fuselage group includes the aft bulkheads. The fins are modeled as point masses on the wing tips. The engines, main landing gear, and nose landing gear are modeled as point masses.

Weight group	Modeled by
Fuel	3 Tank solids
Passengers	Cabin trapezoid
Cargo	Cargo trapezoid
Flight control system	Outer wing solid
Hydraulic and electric systems	Whole wing
Instruments	Point mass
PACKS	Point mass
APU	Point mass
Furnishing	Oval part of fuselage
Outer wing structure	Outer wing solid
Fuselage trailing edge	Trailing edge solid
Nose	Point mass
Aft fuselage	Point mass
Secondary structure	Oval part of fuselage
Fins	Point mass
Engines	Point mass
Main landing gear	Point mass
Nose landing gear	Point mass
Operating items	Oval part of fuselage
Fuselage structure	30 Solids in fuselage

Table 3.3: Weight groups in mass distribution model.

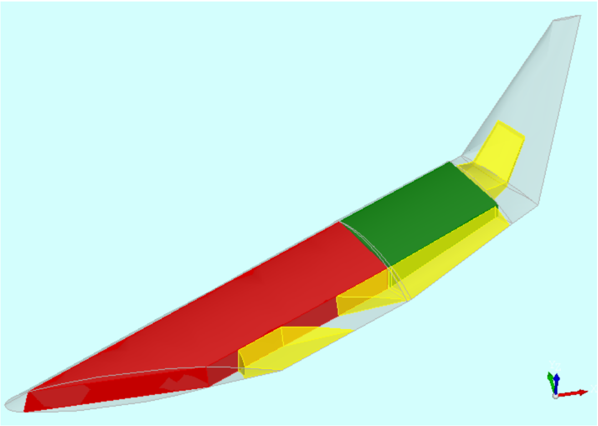

Figure 3.6: Passenger cabin (red), cargo hold (green), and fuel tanks (yellow).

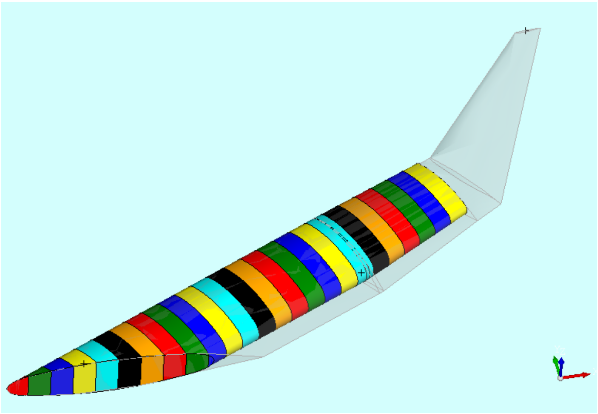

Figure 3.7: Solids representing the fuselage sections.

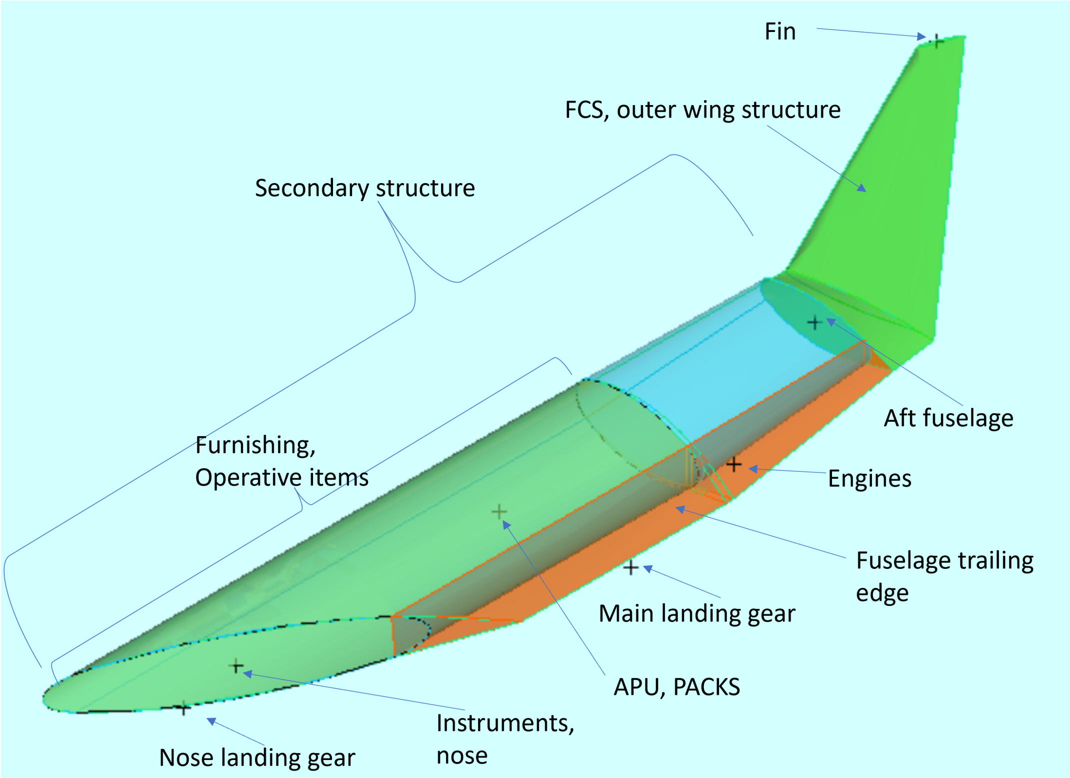

Figure 3.8: Solids and point masses of miscellaneous weight groups. Hydraulic and electric systems and paint are distributed over the whole wing.

3.3.3. Landing Gear and Engine Placement

The nose landing gear is located at x = 6.47 m as determined by Bourget [15] using the coordinate system shown in Figure 3.9. The main landing gear location is crucial for the design of the Flying-V. It must be inside the bandwidth of longitudinal locations that allow for enough take-off rotation power, while keeping the airplane safe from tipping over. This can be achieved by placing it such that the angle between the vertical axis and a line drawn between the most aft center of gravity and the point where the wheel touches the ground is less than 17 degrees, the maximum tipback angle for take-off.

$$x_{\text{mlg}} = x_{\text{cg}_{\text{aft}}} + L_{\text{strut}} \tan(\theta_{\text{tipback}}) \tag{3.16}$$

Since the most aft center of gravity changes with the location of the landing gear, Equation 3.16 is iterated until the locations of the total center of gravity and main landing gear are consistent. The spanwise location of the engines is based on the results of the research of Rubio Pascual [14], who found that drag penalty of the engine integration was minimized at an engine distance from the center axis of around 14.5 % of the half-span with a total span of 65. Since the total span is now variable, the engine placement in meters depends on the total span, but the distance as percentage of the wingspan is kept at 14.5 %. The spanwise distance between the engine and main landing gear is kept at a constant 0.8 m, as done by Oosterom based on the landing gear and fairing design of Bourget.

3.3.4. Passengers and Cargo Compartments

The passengers and cargo are both located in the trapezoidal part of the cabin. First, it needs to be determined which part contains the passengers and which contains the cargo. This is done by first determining the area required for the maximum number of passengers. For this a constant passenger area density of 108 kg/m^2 was used. This value is based on average mass per passenger and the seat layout (aisle width, seat width, seat pitch) used in previous studies [1, 3, 11]. Multiplying this with the height of the cabin gives the required volume. The trapezoid is then split into two parts with the cutting plane perpendicular to the fuselage beam axis. The location of the cutting plane is calculated such that the part on nose side has a volume slightly larger than the required volume of the passenger compartment. The volume available for the cargo follows from the

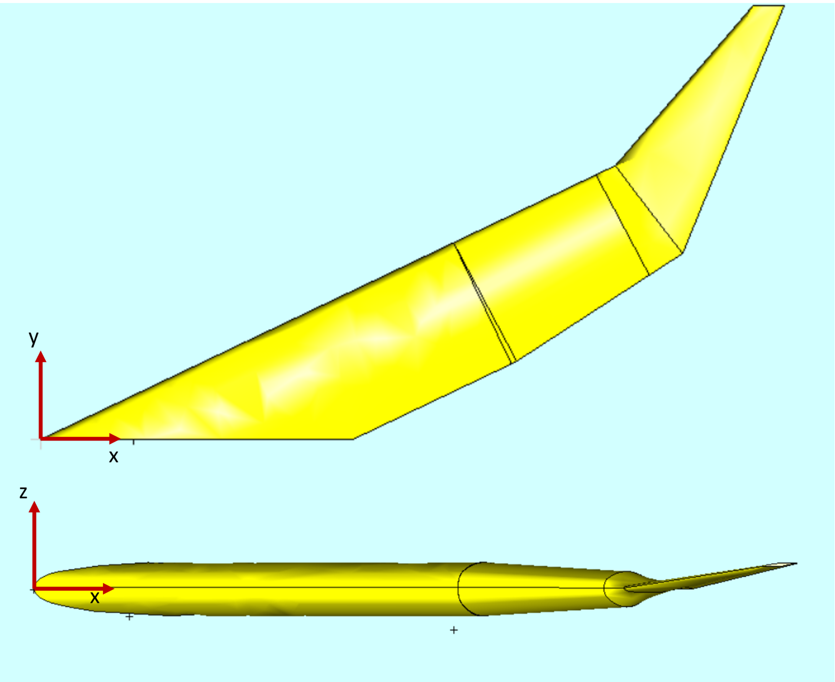

Figure 3.9: Coordinate system and origin used to locate components.

difference between the total trapezoid and the passenger cabin. The maximum cargo mass that can be carried is found by multiplying the cargo compartment volume with a fixed density. This density was determined by dividing the harmonic cargo weight by the volume of the required number of LD-9 containers. For the FV-1000, with an harmonic cargo weight of 33.1 tons in 18 containers of 10.8 m^3, the density multiplied by a scaling factor of 0.88 is 151 kg/m^4. The scaling factor is used to take into account the fact that the square boxes cannot exactly fit in the shape of the cargo compartment, effectively lowering the density and increasing the volume needed.

3.3.5. Fuel and Payload Loading Simulation

The parts that represent the fuel, passengers and cargo need to change in size depending on how the aircraft is loaded. This way, the center of gravity can be calculated for any combination of fuel, passenger and cargo weight. The shape and location of the cargo and passenger volumes should also change depending on whether the mass is loaded front-to-back or back-to-front, since this affects the center of gravity. Furthermore, the volumes representing the fuel should increase or decrease in size depending on the amount of fuel carried in each of the six tanks. The center of gravity can then be calculated for any loading scenario. The loading scenario that is used during the optimization is with the total payload equal to the design payload where passengers take up 84 % of the payload weight and the cargo 16 %.

The solid representing the passenger mass is obtained by shrinking the passenger cabin in a way that the length of the shape is decreased while width and height remain the same. This is possible using CAD operations in ParaPy. The volume of this scaled shape should be proportional to the passenger mass. The volume factor with which the shape is shrunk is equal to the loaded passenger mass divided by the maximum passenger mass (the design payload). The same is done for the cargo.

The volumes of the fuel mass shapes are scaled with respect to the tank volumes in three dimensions based on the fuel weight and density. The center of gravity of the fuel in one tank is approximated to stay equal to the center of gravity of the tank itself, although in reality the center of gravity of the fuel can move due to gravity and the fuel behaving like a fluid. In Figure 3.10 the solids are shown for a scenario where the passenger weight loaded is 47 % of the maximum passenger capacity, the cargo weight is 26 % of the cargo capacity. Both the cargo and passengers are loaded back-to-front. The aft tank is fully filled, the middle tank is partially filled, and the front tank is empty.

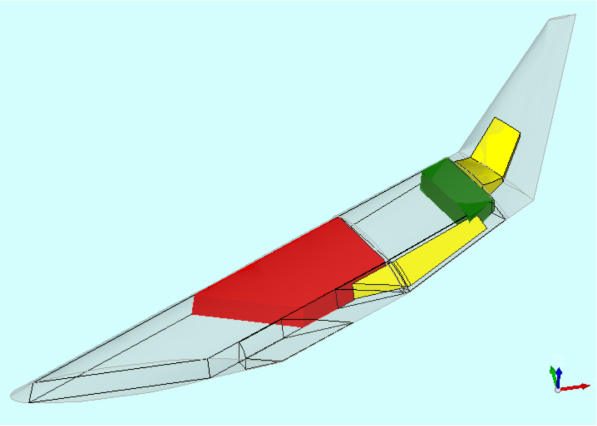

Figure 3.10: Passengers (red), cargo (green), and fuel (yellow) in a specific loading scenario.

3.4. Fuel Loading Strategy

The movement of the center of gravity during loading and unloading can be illustrated in a loading diagram. The center of gravity calculated by the mass distribution module as a function of passenger, cargo, and fuel weight is shown in Figure 3.11. In this case, the design payload weight and fuel weight are used and the total weight is equal to the maximum take-off weight. The passenger and cargo weight are both half of the design payload weight in this example. The center of gravity for both loading directions is shown. It can be seen that the range of possible centers of gravity is quite large. The change in center of gravity due to change in fuel weight of more than three meters is especially large compared to a conventional airplane. This can cause several problems for the flight performance and stability and control. A large shift in center of gravity during flight means that the aircraft cannot fly at the static margin for which it is optimized leading to trim drag penalties, the center of gravity may move too far forward to maintain controllability or too far aft to maintain stability. In order to limit the shift in center of gravity during flight and keep it close or equal to a desired location, a system for active CG control will be used. This means that for a given fuel mass, the distribution of fuel among the tanks is calculated that leads to a total center of gravity as close as possible to a certain desired value. The fuel is continuously pumped between the tanks to maintain the required distribution fuel mass.

The determination of the optimal distribution of fuel among the fuel tanks can be described as a minimization problem. The function that must be minimized is the absolute difference between the desired center of gravity and the total center of gravity of the aircraft. The total center of gravity is obtained by summing the moment around the nose exerted by the zero-fuel mass aircraft and the moments exerted by the three fuel masses, resulting into Equation 3.17. The design variables are the fuel masses m_f in tank 1, tank 2, and tank 3, where the numbering is from nose to tail and the tanks in both wing halves form one tank together. The moment arm r_t is the distance from a tank's center of gravity to the nose. A constraint must be applied to guarantee that the sum of the three fuel masses is equal to the total loaded fuel mass, see Equation 3.18.

$$\text{minimize}: f = \left| x_{\text{cg}_{\text{des}}} - \frac{m_{\text{ZF}} x_{\text{cg}_{\text{ZF}}} + m_{f_1} r_{t_1} + m_{f_2} r_{t_2} + m_{f_3} r_{t_3}}{m_{\text{ZF}} + m_{f_{\text{tot}}}} \right| \tag{3.17}$$

$$\text{subject to}: m_{f_{\text{tot}}} = m_{f_1} + m_{f_2} + m_{f_3} \tag{3.18}$$

$$0 \leq m_{f_{1,2,3}} \leq m_{t_{1,2,3_{\text{max}}}} \tag{3.19}$$

The bounds applied to the design variables follow from the fact that the fuel masses must be larger than zero and smaller than or equal to the maximum fuel mass that fits inside the corresponding tank. The number of constraining equations is not enough to have a single solution for the three fuel masses. To solve this, the optimization is done only for tank 1 and tank 2. Tank 3 is only filled when the other tanks are fuel. A minimizer featuring the SLSQP algorithm is used to calculate the optimal fuel distribution which satisfies the bounds and constraints. The loading diagram that results when the optimal fuel distribution is used, is shown in Figure 3.12. Now the shift in center of gravity caused by change in fuel mass is reduced to 0.8 m. It can also be seen that in this case it is possible to obtain exactly the desired center of gravity for a large range of fuel mass. The fuel distribution required to achieve this for the whole range of fuel mass is shown in Figure 3.13.

Starting at zero fuel weight, the center of gravity has to move more aft, so only tank 2 is filled to achieve this faster. Between 10000 and 60000 kg fuel mass, the amount of fuel in tank 1 and 2 can be balanced to keep the center of gravity at the desired location until tank 1 is full. This range corresponds to the vertical part of Figure 3.12. After this, only tank 2 is filled, moving the center of gravity further aft. Tank 3 is not filled in this case, because the total amount if fuel fits in the first two tanks.

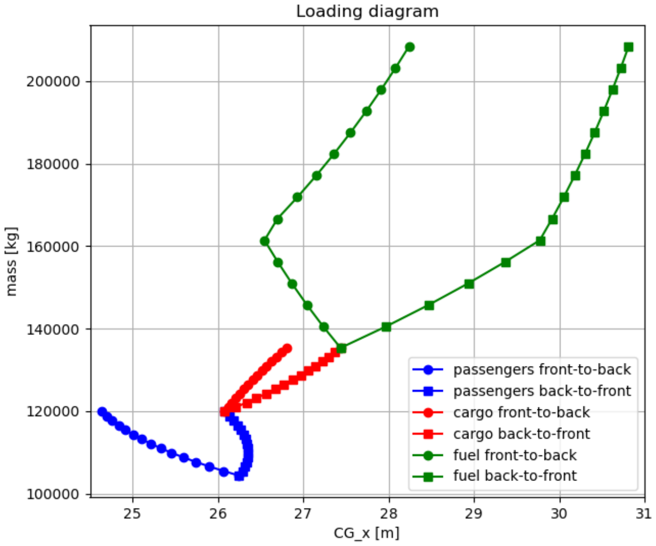

Figure 3.11: Loading diagram without active CG control.

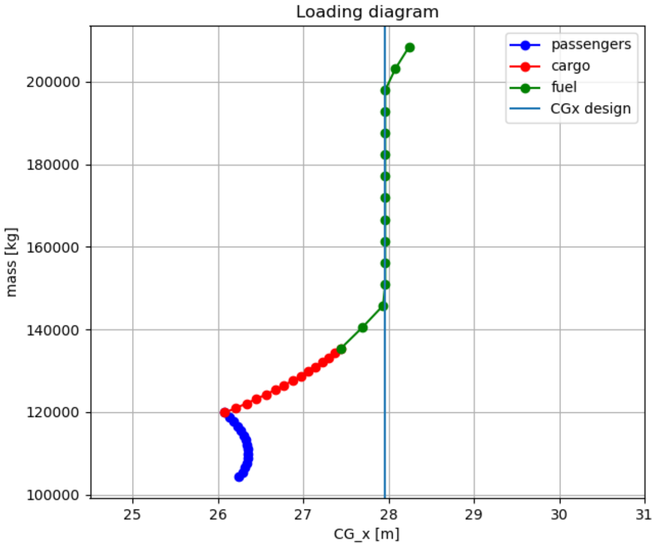

Figure 3.12: Loading diagram with active CG control.

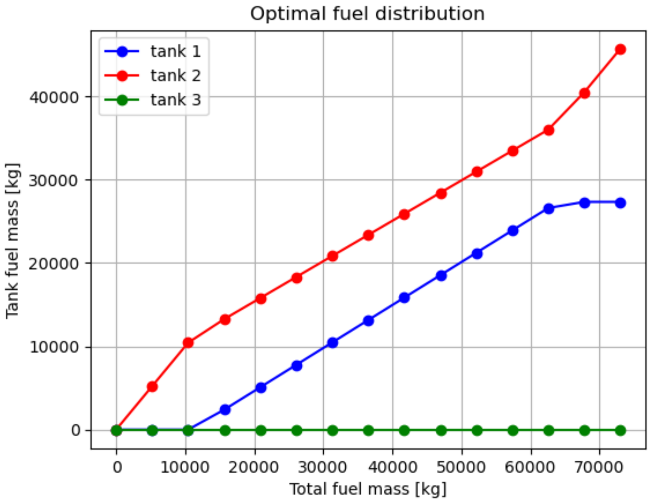

Figure 3.13: Fuel mass distribution for optimal CG at a range of fuel loading.

3.5. Cruise Performance Analysis

The performance of the Flying-V family will be rated in terms of fuel weight needed for the design mission. The design mission is to transport a payload over a certain range. The design payload and range for the three aircraft versions are fixed. The range of an aircraft depends on the aerodynamic efficiency of the airframe, weight, and engine performance. These performance indicators are combined in the Breguet range equation:

$$R = \frac{V}{C_T}\frac{L}{D}\ln\left(\frac{W_{\text{start-cr}}}{W_{\text{end-cr}}}\right) \tag{3.20}$$

The specific fuel consumption C_T depends only the engine is assumed to have a constant value of 14 g/kN/s. This equation can be solved for the fraction of weight at the start cruise and end of cruise $\frac{W_{\text{start-cr}}}{W_{\text{end-cr}}}$. The total mission fuel weight is calculated using Equation 3.21 where the factor 0.938 accounts for the fuel used during warm-up, taxiing, take-off, climb, descent, and landing.

$$W_{\text{fuel,mission}} = \left[1 - 0.938\frac{W_{\text{end-cr}}}{W_{\text{start-cr}}}\right] W_{\text{MTO}} \tag{3.21}$$

The design point for which the airplane is optimized is trimmed cruise flight. The airplane is trimmed when the net forces and moments on the airplane are zero. Longitudinal stability must be ensured, which is the case when C_{m_α} is negative i.e. a positive perturbation in angle of attack leads to a nose-down pitching moment. An important factor related to trim and static longitudinal stability and controllability is the static margin. It is the distance between the the neutral point and center of gravity. In Equation 3.22 x_{np} and x_{cg} are the distance of the neutral point and center of gravity measured from the datum.

$$SM = \frac{x_{\text{np}} - x_{\text{cg}}}{\bar{c}} \tag{3.22}$$

The neutral point is the streamwise location about which the pitching moment coefficient invariant with angle of attack. Placing the center of gravity on the neutral point leads to a neutrally stable aircraft or a C_{m_α} equal to zero. The relation between static margin, pitching moment derivative, and lift curve slope is obtained by taking the sum of moments about the center of gravity and differentiating with respect to the angle of attack, leading to the equation:

$$SM = -\frac{C_{m_\alpha}}{C_{L_\alpha}} \tag{3.23}$$

Knowing that the lift curve slope C_{L_α} is positive and looking at the signs of Equation 3.22 and Equation 3.23 it becomes clear that to keep the aircraft longitudinally stable, the center of gravity should be placed ahead of the neutral point. However, placing the the center of gravity too far forward can be detrimental to the longitudinal controllability of the aircraft. The location of the center of gravity also has an effect on the the amount of control surface deflection needed to trim the aircraft. Depending on the sign of the pitching moment coefficient at the trim angle of attack, the control surface deflection is either positive or negative. The control surface deflections for trim should not be too large, since this generates additional induced drag called trim drag. For the design point, a static margin of $0.06\bar{c}$ is used, the same value as chosen by Faggiano [11] for aerodynamic optimization. The location of the neutral point is calculated by an aerodynamic solver and the static margin is subtracted to obtain the design center of gravity. The average lift during cruise is estimated using the semi-empirical relation:

$$L_{\text{des}} = \sqrt{W_{\text{MTO}}(W_{\text{MTO}} - W_{\text{fuel}})} \tag{3.24}$$

The lift coefficient and pitching moment coefficient in trim:

$$C_{L_{\text{trim}}} = \frac{L_{\text{des}}}{qS} \tag{3.25}$$

$$C_{m_{\text{cg}}} = 0 \tag{3.26}$$

The angle of attack α_{trim} and elevator deflection $\delta_{e_{\text{trim}}}$ required to trim the aircraft with the center of gravity at the desired static margin are solved for using the aerodynamic model. The drag coefficient generated at the trim angle of attack and elevator deflection also follow from the aerodynamic solver. The trimmed lift-to-drag ratio which will be used to estimate design fuel weight is thus:

$$\left(\frac{L}{D}\right)_{\text{trim}} = \frac{C_{L_{\text{trim}}}}{C_{D_{\text{trim}}}} \tag{3.27}$$

3.6. Control Authority Assessment

Stability and control considerations are usually dictated by federal regulations such as EASA's CS-25 Certification Specifications and Acceptable Means of Compliance for Large Aeroplane Subpart B - Flight [28]. In this study, the assessment of control authority provided by the control effectors is based on the methods used in critical studies in stability and control analysis for conceptual design such as those by Roskam [29], Kay [30], and Lee. These methods mainly consist of identifying the design-critical controllability criteria and most critical flight conditions. The control authority criteria are derived from the regulations and past experience. The flight conditions are variables that influence the aerodynamic coefficients or inertia of the aircraft. These variables are: weight, CG location, engine setting, altitude, and speed.

The equations of motion in combination with the stability and control derivatives are used to the calculate control surface deflection required for steady trim and maneuvers. The required control surface deflections should be smaller than the maximum angle at which the control surface is effective, which is assumed to be about 25 degrees. The derivation of the equations of motion can be found in many flight dynamics text books, like Etkin [31]. In this section, the selected controllability requirements are explained and it is shown how they are evaluated and converted to design constraints.

3.6.1. Longitudinal Trim

Steady level 1-g flight must be attainable at all service altitudes and all speeds between stall speed and maximum speed. The elevator is used to balance the longitudinal forces and moments. The equations for trimmed lift coefficient and moment equilibrium are:

$$C_{L_{\text{trim}}} = \frac{W}{qS} = C_{L_0} + C_{L_\alpha}\alpha_{\text{trim}} + C_{L_{\delta e}}\delta_{e_{\text{trim}}} \tag{3.28}$$

$$C_m = 0 = C_{m_0} + C_{m_\alpha}\alpha_{\text{trim}} + C_{m_{\delta e}}\delta_{e_{\text{trim}}} \tag{3.29}$$

The equations are solved for the trim angle of attack and elevon deflection. The constraint is satisfied when the required deflection angle is smaller than the maximum deflection angle and the angle of attack is smaller than the angle at which pitch break is expected to occur, around 20 degrees based on previous studies.

3.6.2. Pull-up Maneuver

In in Acceptable Means of Compliance to Subpart B of the CS-25 Amendment 26 [28], the minimum maneuvering capability is specified in Section 6. Starting from trimmed 1-g flight, the airplane must be able to pull up to a load factor of 1.3 with a change in elevator deflection and angle of attack within the effective range. The most limiting conditions for this constraint are at the approach speed and with the center of gravity most forward. The additional lift coefficient required for the pull-up maneuver to n number of g's and associated non-dimensional pitch rate are given by Equation 3.30 and Equation 3.31.

$$\Delta C_L = \frac{\Delta L}{qS} = \frac{(n-1)W}{qS} \tag{3.30}$$

$$\hat{q} = \frac{(n-1)\bar{c}g}{2V^2} \tag{3.31}$$

The change in lift pitching moment for trimmed flight:

$$\Delta C_L = C_{L_\alpha}\Delta\alpha + C_{L_q}\hat{q} + C_{L_{\delta e}}\delta_e \tag{3.32}$$

$$\Delta C_m = 0 = C_{m_\alpha}\Delta\alpha + C_{m_q}\hat{q} + C_{m_{\delta e}}\delta_e \tag{3.33}$$

Combining Equation 3.30 through Equation 3.33 gives the two equations that need to be solved for $\Delta\alpha$ and $\Delta\delta_e$:

$$C_{L_\alpha}\Delta\alpha + C_{L_{\delta e}}\delta_e = (n_z - 1)\left[\frac{W}{qS} - C_{L_q}\frac{g\bar{c}}{2V^2}\right] \tag{3.34}$$

$$C_{m_\alpha}\Delta\alpha + C_{m_{\delta e}}\Delta\delta_e = -(n_z - 1)C_{m_q}\frac{g\bar{c}}{2V^2} \tag{3.35}$$

3.6.3. Steady Sideslip

Directional and lateral control requirements are specified in CS-25.147 and CS-25.149. The aircraft should be able to maintain steady sidelip using the aileron and rudder. This means that when the aircraft is flying at a sideslip angle β, yawing and rolling moments and the sideforce should become zero, such that steady straight flight is maintained. The sideslip angle that must be maintained is based on the maximum crosswind specified in CS-25.237, which comes down to a sideslip of around 11 degrees. Compliance with this requirement must be shown at minimum control speed and maximum take-off weight. Trim is achieved using a certain combination of aileron and rudder deflection and bank angle. The required combination must be acceptable in terms maximum control power. The equations for sideforce, rolling, and yawing moments are written down:

$$C_{Y_\beta}\beta + \frac{W}{qS}\cos(\gamma)\phi + C_{Y_{\delta r}}\delta_r + C_{Y_{\delta a}}\delta_a = 0 \tag{3.36}$$

$$C_{l_\beta}\beta + C_{l_{\delta r}}\delta_r + C_{l_{\delta a}}\delta_a = 0 \tag{3.37}$$

$$C_{n_\beta}\beta + C_{n_{\delta r}}\delta_r + C_{n_{\delta a}}\delta_a = 0 \tag{3.38}$$

Equation 3.37 and Equation 3.38 can be solved together for the deflection angles δ_r and δ_a and Equation 3.40 can be solved for the bank angle ϕ. The bank angle must less than 5 degrees as specified by the airworthiness authorities and the required rudder and aileron deflections must be within the maximum effective range.

3.6.4. Engine-Out Trim

Lateral/directional trim and straight flight must be maintained when one engine is inoperative and causing asymmetric thrust. This must be possible at minimum control speed and maximum take-off weight. The yawing moment produced by the inoperative engine is calculated by using the take-off thrust and the distance of the engine to the longitudinal axis and the value is nondimensionalized. Here the drag generated by the windmilling engine is neglected.

$$C_{n_{\mathrm{OEI}}} = \frac{N_{\mathrm{OE}}}{qS} = \frac{-0.5T_{\mathrm{TO}}y_e}{qS} \tag{3.39}$$

The equations for sideforce and lateral and directional trim are:

$$\frac{W}{qS}\cos(\gamma)\phi + C_{Y_{\delta r}}\delta_r + C_{Y_{\delta a}}\delta_a = 0 \tag{3.40}$$

$$C_{l_{\delta r}}\delta_r + C_{l_{\delta r}}\delta_r = 0 \tag{3.41}$$

$$C_{n_{\delta r}}\delta_r + C_{n_{\delta r}}\delta_r + C_{n_{\mathrm{OEI}}} = 0 \tag{3.42}$$

The three equilibrium equations can be solved for the rudder and elevon deflection angles and bank angle.

3.6.5. Time-to-Bank

With the airplane in trim, it must be possible from a steady 30 degrees banked turn, to roll to a 30 degrees bank angle in the opposite direction in 7 seconds. This is the acceptable method to demonstrate compliance with CS-25.147(d). The rudder may be used to minimize sideslip. The most demanding conditions are approach speed and maximum landing weight, with the most aft CG. Knowing the maximum aileron deflection angle and assuming a step input of the ailerons, the time to reach a specified roll angle can be calculated using a simulation of the motion. The equations for roll rate and rolling acceleration are given by ordinary differential equations:

$$\dot{\phi} = p \tag{3.43}$$

$$\dot{p} = \frac{qSb}{I_{xx}} \left[(C_{l_{\delta a}} \delta_a) + (C_{l_p} p) \left(\frac{b}{2V} \right) \right] \tag{3.44}$$

An analytic expression can has been derived by Kay [30] for the roll rate and this can be integrated to obtain the formula for the calculation of the bank angle as function of time:

$$\phi(t) = -\frac{2V}{b} \frac{C_{l_{\delta a}} \delta_a}{C_{l_p}} \left[t + \frac{1}{L_p} \left(1 - e^{\frac{qSb^2}{2VI_{xx}} C_{l_p} t} \right) \right] \tag{3.45}$$

The above equation can be used to determine whether the aircraft can roll the required bank angle in the specified amount of time and if the angle is at least 60 degrees the constraint is satisfied.

3.6.6. Take-off Rotation

Pitch control input is given once the aircraft reaches rotation speed. This rotation speed can be calculated as the speed at which the dynamic pressure is high enough for the nose wheel to lift off from the ground. This speed can be calculated by considering the moment equilibrium about the main landing gear wheel. The moment caused by gravity must be countered by the aerodynamic moments. The moment coefficient in Equation 3.46 is taken about the main gear wheel. This coefficient contains the effect of the elevon deflection and angle of attack. The elevons are deflected upwards to their maximum angle of 30 degrees. The angle of attack on the ground is equal to -3 degrees based on the strut lengths of the nose and main landing gear. The most critical condition is at maximum take-off weight and the CG at the most forward location. The rotation speed must be smaller than the minimum take-off safety speed $V_{2_{\text{min}}}$ plus the speed gained before reaching a height of 11 m as specified in CS-25.107. The minimum take-off safety speed is the speed at which the aircraft may safely climb with one engine inoperative.

$$V_{\text{R}} = \sqrt{\frac{2W(x_{\text{cg}} - x_{\text{mlg}})}{-\rho S \bar{c} C_{m_{\text{mlg}}}}} \tag{3.46}$$

3.6.7. Control Departure

The aerodynamic behaviour at high angle of attack is difficult to calculate using the low fidelity tools used in this research. However, there are several parameters that can be used for the estimation of the airplane's susceptibility to loss of control at high angle of attack operation. The open loop directional stability or can be estimated using the parameter $C_{n_{\beta_{\text{DYN}}}}$. When it is greater than zero for the angle of attack range, little yaw departure tendency can be expected.

$$C_{n_{\beta_{\text{DYN}}}} = C_{n_\beta} \cos(\alpha) - \frac{I_{zz}}{I_{xx}} C_{l_\beta} \sin(\alpha) \tag{3.47}$$

To assess the spin resistance and susceptibility to roll departure due to the ailerons, the Lateral Control Departure Parameter is used. Departure tendency is small when the value is greater than zero.

$$\text{LCDP} = C_{n_\beta} - \frac{C_{n_{\delta a}}}{C_{l_{\delta a}}} C_{l_\beta} \tag{3.48}$$

The parameters $C_{n_{\beta_{\text{DYN}}}}$ and LCDP depend on the angle of attack. Since control departure must be avoided for the range of angles of attack that the aircraft flies at, they are evaluated until 20 degrees angle of attack. It is assumed that pitch break occurs around this angle based on previous research [2] and is therefore used as maximum angle of attack.

3.6.8. Summary of Control Requirements

An overview of control constraints is shown in Table 3.4. The constraints are evaluated at sea level and low speed. Most constraints need to be satisfied as approach speed, but for the directional/lateral control constraints there is a minimum control speed at which the aircraft should have sufficient lateral and directional control. The approach speed is used in combination with maximum landing weight. The maximum landing weight is estimated by multiplying a constant factor of 0.76 with the maximum take-off weight. The factor is the same as the one used by Oosterom [3] who used Airbus data to estimate an average maximum landing weight as a fraction of maximum take-off weight. The other speeds are used in combination with maximum take-off weight. The stall speed in take-of conditions V_{S0} is calculated using an estimated maximum lift coefficient of 1.1 taken form the study of Bourget [15]. The minimum control speed V_{mc} is taken as 1.2 times the stall speed. The minimum take-off safety speed is taken as 1.1 times V_{mc}.

A control constraint is usually critical at either most forward or aft center of gravity. However, the center of gravity location also depends on the total weight. The control requirements are evaluated at maximum take-off weight (MTOW) and maximum landing weight (MLW). The center of gravity corresponding to the weights in question can be found using the loading as shown in Figure 3.14.

Criterion	Speed	Weight and CG	Constraint
Longitudinal Trim	V_{app}	MLW	$\delta_e < \delta_{e_{max}}$, $\alpha < \alpha_{max}$
Pull-up maneuver	V_{app}	MLW	$\delta_e < \delta_{e_{max}}$, $\alpha < \alpha_{max}$
Steady Sideslip	V_{mc}	MTOW	$\delta_r < \delta_{r_{max}}$, $\delta_a < \delta_{a_{max}}$, $\phi < \phi_{max}$
Engine-Out Trim	V_{mc}	MTOW	$\delta_{r_{max}}$, $\delta_a < \delta_{a_{max}}$, $\phi < \phi_{max}$
Time-to-bank	V_{app}	MLW	$\phi > \phi_{min}$
Take-off rotation	V_{R}	MTOW	$V_{\mathrm{R}} < V_{2_{\mathrm{min}}}$ - 5
Control Departure	V_{S0}	MTOW	$C_{n_{\beta_{\mathrm{DYN}}}} > 0$, LCDP > 0

Table 3.4: Control requirements and critical conditions in which they must be evaluated.

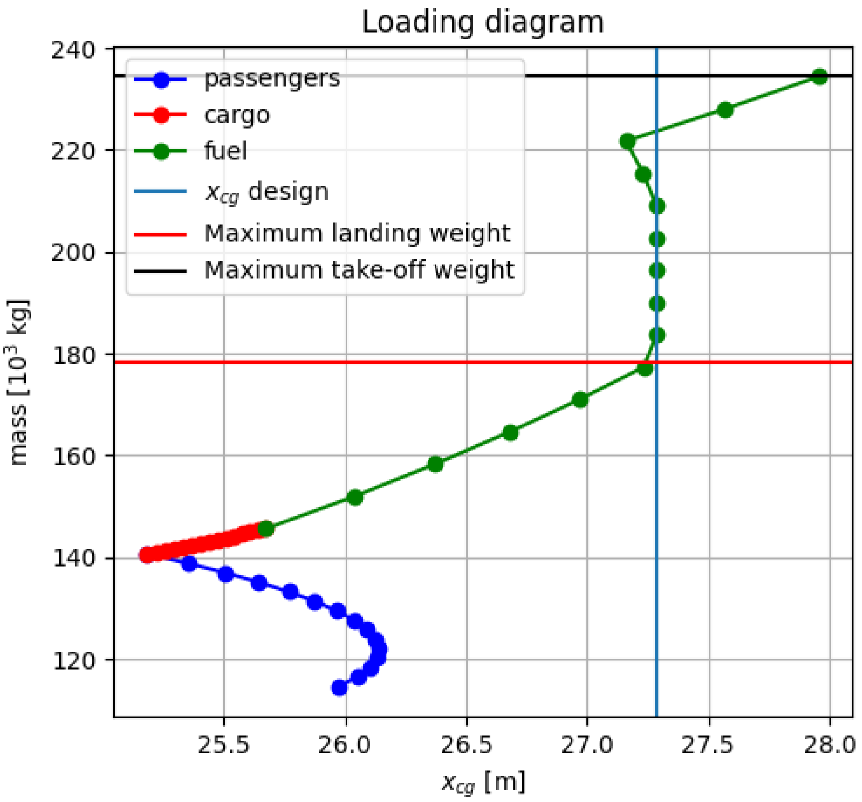

Figure 3.14: Loading diagram for FV-900. Center of gravity locations corresponding to weight e.g. MTOW and MLW can be read.

4

Verification and Validation

4.1. Stability and Control Derivatives

The stability and control derivatives predicted by *VORLAX* will be validated against experimental data. A flight test of a Flying-V sub-scale model has been done by Ruiz Garcia et al. [6]. The data obtained during this experiment were used to identify an aerodynamic model. This model can be used to estimate the aerodynamic coefficients by means of a systems of equations. The model is valid for the scaled model flying at a low Reynolds and Mach number. The sub-scale model used during the experiment is modeled in *VORLAX* using the planform dimensions shown in Figure 4.1.

Differences between the vortex lattice solver results and experimental values are expected: The effect of thickness is not modeled in the solver, since the modeled geometry consists of flat panels. In reality, the inboard part of the Flying-V has a relatively high thickness-to-chord ratio. The possibly destabilizing effect of this thickness around the yaw axis is ignored by the solver. The flight test model has engines and extended landing gear which are not modeled in the vortex lattice solver. The effect of viscosity is not present in the vortex lattice solver, leading to an infinite Reynolds number as opposed to the relatively low Reynolds number during the experiment. The experiments done by Anyoji et al. have shown that the control surface effectiveness is smaller at low deflection angles (smaller than 5 degrees) and the detrimental effect to control surface effectiveness of lower Reynolds numbers is larger for thick airfoils [32]. The effectiveness of control surfaces may be over-estimated by the vortex lattice solver, since Reynolds number dependent effects such as flow separation are not taken into account.

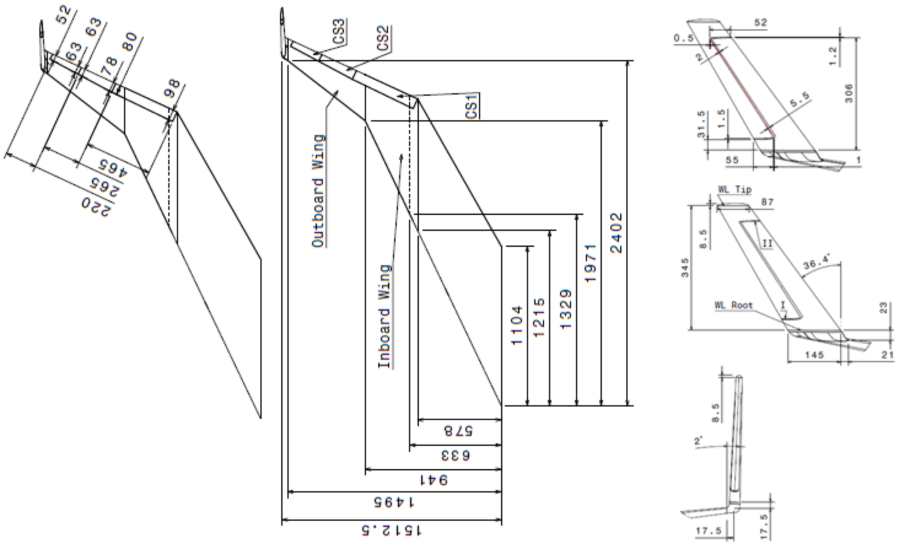

Figure 4.1: Dimensions of the sub-scale model [4]

4.1.1. Comparison of Coefficients

The coefficients calculated by the identified model are given in the body axes, whereas the *VORLAX* results are given in the wind axes, see Figure 4.2. Before comparing the coefficients, they need to be in the same reference frame. To convert the experimental results to the wind axis system, the vector of coefficients is multiplied by a transformation matrix T_{ab} containing the angle of attack and sideslip angle. The subscripts in T_{ab} refer to aerodynamic (wind axes) and body axis frame.

$$T_{\text{ab}} = \begin{bmatrix} \cos(\beta)\cos(\alpha) & \sin(\beta) & \cos(\beta)\sin(\alpha) \\ -\sin(\alpha)\cos(\alpha) & \cos(\beta) & -\sin(\beta)\sin(\alpha) \\ -\sin(\alpha) & 0 & \cos(\alpha) \end{bmatrix} \tag{4.1}$$

$$\begin{bmatrix} C_D \\ C_Y \\ C_L \end{bmatrix} = T_{\text{ab}} \begin{bmatrix} -C_X \\ C_Y^b \\ -C_Z \end{bmatrix} \tag{4.2}$$

$$\begin{bmatrix} C_l \\ C_m \\ C_n \end{bmatrix}^a = T_{\text{ab}} \begin{bmatrix} C_l \\ C_m \\ C_n \end{bmatrix}^b \tag{4.3}$$

The stability and control derivatives calculated by *VORLAX* and the the identified model are presented in Table 4.1. The lift slope C_{L_α} and are $C_{L_{\delta e}}$ are the are close to the experimental values. The lift and the elevon effect on the total lift are accurately predicted by *VORLAX*. The computed rolling and yawing moment derivatives with respect to the elevon and rudder deflections ($C_{l_{\delta r}}$, $C_{l_{\delta a}}$, $C_{n_{\delta r}}$, $C_{n_{\delta a}}$) are all larger than the experimental values, which is probably due to the boundary layer effects that are not present in the VLM analysis. The side-force derivative C_{Y_β} is much higher in magnitude in the experiment. After all, the side force in sideslip generated by the thick inboard wing, landing gear, and engine nacelles are not evaluated by *VORLAX*, it is only the fins that generate a sideforce. This effect could also partly explain the difference in directional stability C_{n_β}. The difference in derivatives with respect to the angular rates are quite large, but the accuracy of the vortex lattice solver in computing these dynamic derivatives is difficult to determine, while the angular rates have been measured during the experiment using sensors in the autopilot. Thus, the computed values of C_{L_q}, C_{m_q}, and C_{l_p} are probably not accurate. A notable difference is seen between the computed and experimental pitching moment stability derivative C_{m_α}. The computed C_{m_α} is higher in magnitude than the experimental value. This indicates that the predicted location of the neutral point is too far (aft/fwd).

4.1.2. Correction Methods

The differences between the VLM results and experiment will be used to derive correction factors to include the thickness and viscosity effects to the calculated derivatives.

The location of the moment reference point needs to be corrected in a way that the calculated neutral point and C_{m_α} is the same as in the experiment. The C_{m_α} as function of moment reference point is plotted in Figure 4.3. The moment reference point used in the experiment is the center of gravity which is located at 1.31 m from the nose. To obtain the required C_{m_α}, the moment reference point should be moved aft to 1.41 m. The shifted distance is equal to 12.5 % of the mean aerodynamic chord $\bar{c}$. In the analysis of the full scale aircraft, the input moment reference point for the calculation of pitching moment will be:

$$x_{\text{ref}} = x_{\text{cg}} + 0.125\bar{c} \tag{4.4}$$

In Equation 4.4, x_{cg} is the center of gravity location calculated by the mass distribution model. The same method for the correction of the pitching moment coefficient can also be used for the yawing moment. Now the moment reference point is shifted by the different distance in order to obtain the correct directional neutral point and C_{n_β}.

The corrections to be added to the remaining stability and control derivatives are calculated based on the difference between the experimental and computational results of the scaled model. Since the Reynolds number of the full scale aircraft in flight is much higher than during the experiment, the added correction Δ_{exp} is first multiplied by a factor f between 0 and 1, to account for the fact that the computational results become more accurate due to the increased Reynolds number. The closer the factor is to 1, the larger the influence of the experimental results. To determine the influence factors, for each coefficient it is decided whether the computational or experimental result is more optimistic for the stability and control performance of the aircraft. For example, the VLM predicts a much larger aileron adverse yaw $C_{n_{\delta a}}$, but it also predicts a higher roll control power $C_{l_{\delta a}}$. The conservative approach is to choose the most pessimistic option and let the factor be 1/3 in case the computational result is more pessimistic and 2/3 in the opposite case. When the experimental results are clearly more accurate, a factor of 1 is used and when no correction is needed, the influence factor is zero. Table 4.2 shows which corrections will be applied to the stability and control derivatives in further analysis.

$$\Delta_{\text{exp}} = C_{\text{experiment}} - C_{\text{calculated}} \tag{4.5}$$

$$C_{\text{corrected}} = C_{\text{calculated}} + f \cdot \Delta_{\text{exp}} \tag{4.6}$$

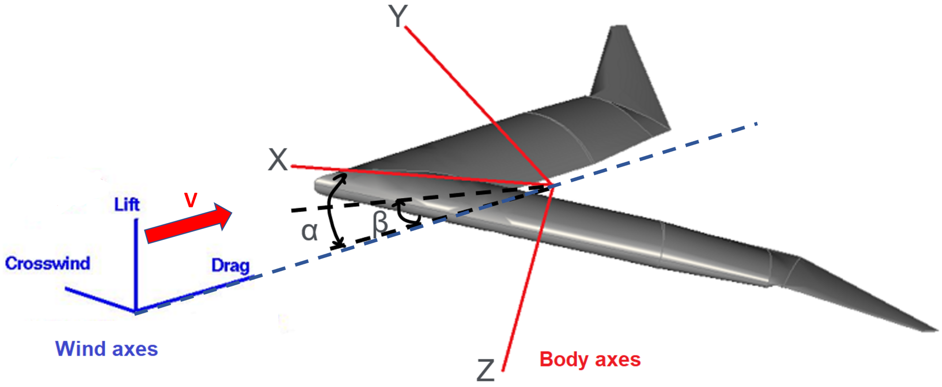

Figure 4.2: Wind axis system used in VORLAX and body axis used in experimental model.

Coefficient	VORLAX	Experiment [6]	% deviation
C_{L_α}	2.779	2.752	-0.99
$C_{L_{\delta e}}$	0.558	0.571	2.20
C_{L_q}	2.690	4.147	54.1
C_{m_α}	-0.612	-0.264	-56.8
$C_{m_{\delta e}}$	-0.561	-0.279	-50.2
C_{m_q}	-2.776	-1.193	-57.0
C_{Y_β}	-0.184	-0.474	157.6
$C_{Y_{\delta r}}$	-0.113	-0.088	-21.8
$C_{Y_{\delta a}}$	0.073	0.089	21.1
C_{l_β}	-0.092	-0.081	-10.7
$C_{l_{\delta r}}$	-0.013	-0.010	-21.1
$C_{l_{\delta a}}$	0.174	0.113	-35.1
C_{l_p}	-0.273	-0.200	-26.5
C_{n_β}	0.077	0.055	-28.2
$C_{n_{\delta r}}$	0.049	0.020	-58.2
$C_{n_{\delta a}}$	-0.026	-0.007	-74.0

Table 4.1: Stability and control derivatives of the sub-scale Flying-V model. Computational and experimental results, $x_{\text{ref}} = 34\ \%\bar{c}$.

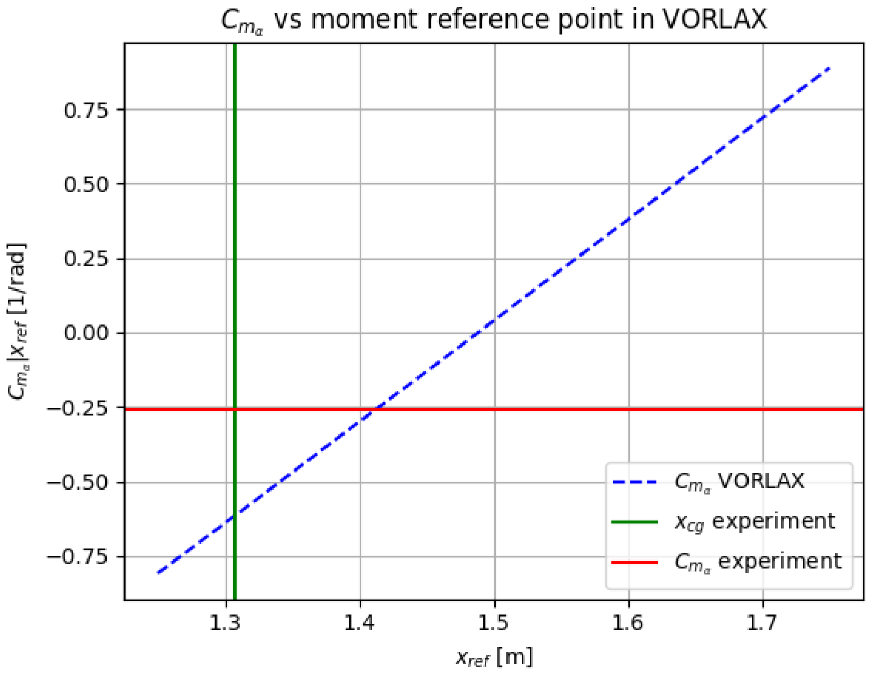

Figure 4.3: Pitching moment derivative as function of moment reference point of the scaled model in VORLAX. CG location of the experimental model indicated by vertical line and experimental C_{m_α} about CG indicated by horizontal line.

Coefficient	Influence factor f
C_{L_α}	None
$C_{L_{\delta e}}$	None
C_{L_q}	1
C_{m_α}	None
$C_{m_{\delta e}}$	2/3
C_{m_q}	1
C_{Y_β}	1
$C_{Y_{\delta r}}$	1/3
$C_{Y_{\delta a}}$	2/3
C_{l_β}	1/3
$C_{l_{\delta r}}$	2/3
$C_{l_{\delta a}}$	2/3
C_{l_p}	1
C_{n_β}	None
$C_{n_{\delta r}}$	2/3
$C_{n_{\delta a}}$	1/3

Table 4.2: Corrections applied to the stability and control derivatives.

4.2. Weight Model Simplification

The weight estimation has been modified to obtain results faster. The calculation of outer wing and fuselage mass is simplified by calculating the mass densities of the fuselage sections and outer wing using the weight results of the initial design vector. The densities have been calculated for the initial FV-900 design, and these have been used for the weight estimation of other geometries. The resulting operative empty weight of the simplified model for different fuselage lengths are compared to the results of Oosterom in Table 4.3. The results for the FV-900 are of course the same, and the results for the FV-800 and FV-1000 are off by 0.1 and 1.6 % respectively. This is considered close enough for the purposes of this research.

Aircraft	Length: L_1 [m]	OEW [10^3 kg] simplified model	full model [3]
FV-900	24.0	115	115
FV-800	18.0	99.8	99.9
FV-1000	29.0	127	129

Table 4.3: Comparison between operative empty weight calculated by simplified and full weight model for different fuselage and outer wing length combinations and all other inputs kept equal.

4.3. Volume Estimation

The mass distribution model uses the volumes of the shapes in the aircraft. The volumes are calculated by ParaPy using the CAD model, but it needs to be checked whether they are calculated correctly. The fuselage cross-section contains two horizontal and vertical walls as shown in Figure 2.6. The three-dimensional shape formed by these walls is shown in Figure 4.4. The passengers and cargo are placed in this shape. This shape will be used to verify the volume calculation by comparing it with the results of manual calculations.

The shape approximately consists of a trapezoidal prism and a rectangular frustum. The volume of the prism is calculated using Equation 4.8 with the area of the base given by Equation 4.7.

$$A_{\text{prism}} = w_1 \left(L_1 - \frac{w_1}{2 \tan \Lambda_{\text{in}}} \right) \tag{4.7}$$

$$V_{\text{prism}} = A_{\text{prism}} h_1 \tag{4.8}$$

The volume of the frustum is calculated by multiplying the Heronian mean of the two bases A_1 and A_2 with the height, as shown in Equation 4.11.

$$A_1 = h_1 w_1 \tag{4.9}$$

$$A_2 = h_3 w_3 \tag{4.10}$$

$$V_{\text{frustum}} = \frac{L_3}{3} \left(A_1 + \sqrt{A_1 A_2} + A_2 \right) \tag{4.11}$$

The input height and widths and the resulting volumes are presented in Table 4.4. The subscripts 1 and 3 refer to the sections shown in Figure 2.5. The difference between the manual calculation and 3D model results is about 4.7 %. The difference can be be explained by the fact that the shapes or not exactly a prism and a frustum. The two bases of the prism are not exactly equal, because the width is not constant along the height of the prism as assumed (the widths used are the widths at 0.6 m from the floor). The small part between the two volumes is also neglected. Thus, the accuracy of the volume calculation is deemed acceptable.

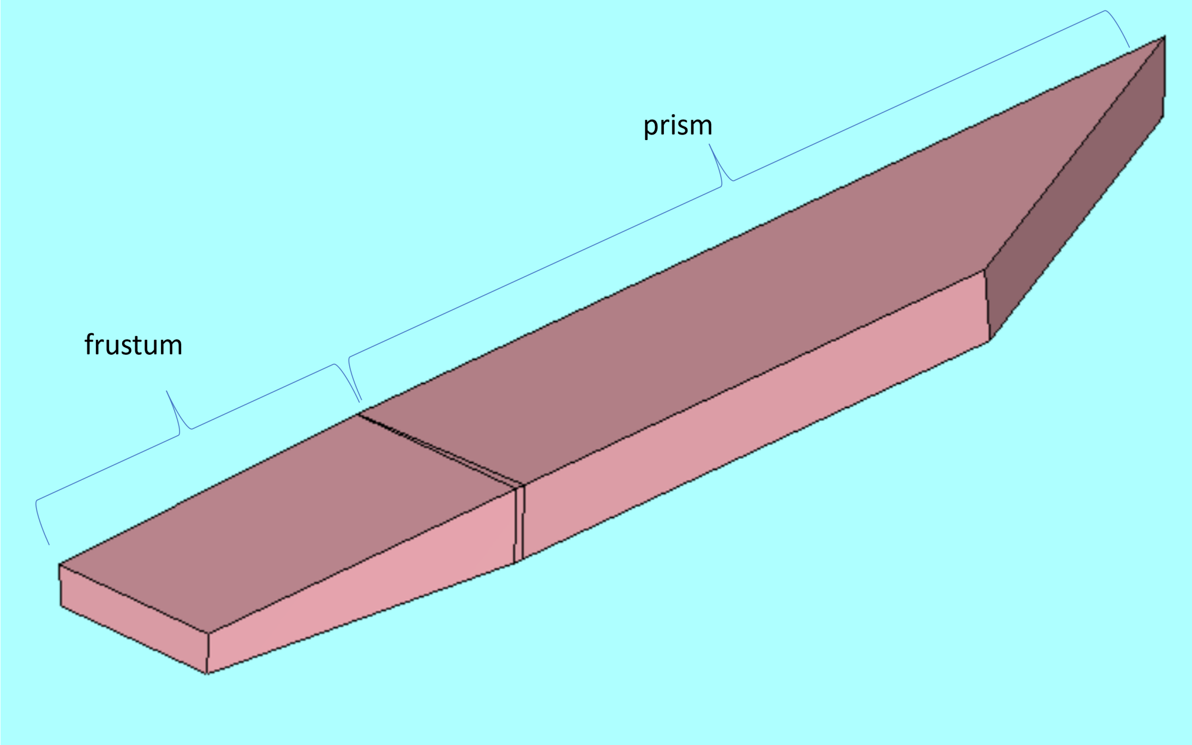

Figure 4.4: Shape formed by the cabin walls containing passengers and cargo.

Length	Description	[m]
h_1	Cabin height at section 1	2.25
h_3	Cabin height at section 3	1.22
w_1	Cabin width at section 1	6.2
w_3	Cabin width at section 3	5.8
L_1	Untapered cabin length	24
L_3	Tapered cabin length	11
	Volume	[m^3]
	Manual calculation	428
	CAD model	448

Table 4.4: Inputs to the calculation of the volume between the fuselage walls and results.

4.4. Moment of Inertia

The moments of inertia calculated by the mass distribution model are compared with the results of previous studies. The moments of inertia have been estimated by Cappuyns for a Flying-V similar to the current FV-1000. Comparisons between these moments of inertia and the ones calculated by the mass distribution model using the the FV-1000 geometry from Oosterom are shown in Figure 4.5 and Figure 4.6. The moments of inertia are evaluated at both maximum take-off weight and operative empty weight. Differences are expected due to the differences in total mass and mass distribution between the two models. However, the order of magnitude of the moments of inertia are the same and there is a similar proportion between the $x-$, $y-$, and $z-$components.

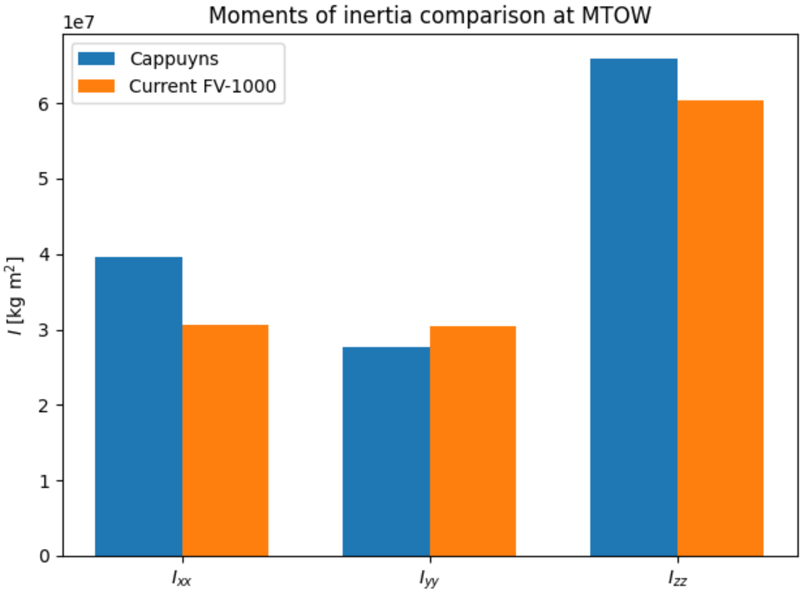

Figure 4.5: Moments of inertia of Cappuyns [5] compared to calculated moments of inertia of current FV-1000 at maximum take-off weight.

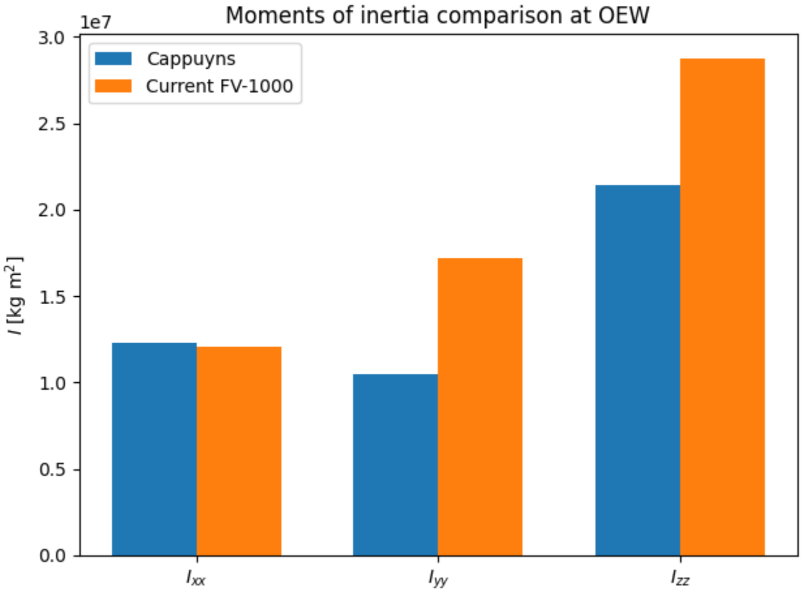

Figure 4.6: Moments of inertia of Cappuyns [5] compared to calculated moments of inertia of current FV-1000 at operative empty weight.

4.5. Sensitivity Analysis

To discover the effect of changing a design variable on the objective function and constraints, a sensitivity analysis is performed. For the objective function and all constraints, partial derivatives with respect to the design variables are calculated using an upwind finite difference.

$$\frac{df}{dx} = \frac{f(x+\Delta x) - f(x)}{\Delta x} \tag{4.12}$$

The logarithmic sensitivity is taken to recognise the relative strengths of the parameters.

$$\frac{d_L f}{d_L x} = \left|\frac{x}{f}\right| \frac{df}{dx} \tag{4.13}$$

The resulting sensitivities are displayed in the sensitivity matrix in Figure 4.7. When the partial derivative is negative, i.e. an increase in a design variable causes a decrease in the function, the cell representing this sensitivity is blue. When the partial derivative is positive the cell is red. The darker the color, the higher the sensitivity. Note that the constraint is satisfied when its sign is positive, so a red sensitivity means that increasing this value (at least starting from the initial design vector) is beneficial for constraint compliance. Increasing fuselage length and outer wing length for example impedes compliance with the maximum span constraint (constraint 18). Increasing the fin length has a positive effect on the rudder power constraints 5 and 8, while increasing the length of the untapered part of the cabin (length 1) has a negative effect. The fin length also positively affects LCDP and directional stability (constraints 14 and 17). The sensitivities for longitudinal control power and longitudinal stability (constraints 2 and 15) have opposite signs. Increasing sweep of the outer wing has a negative effect on the take-off rotation speed, since the elevon hinge line is at a larger angle with respect to the incoming flow. Increasing the lengths of the fuselage and outer wing also decreases the fuel weight due to the added empty weight. It should however be noted that the sensitives are only calculated around the initial design vector. When the design vector is changed, the sensitivities may decrease, increase, or change in sign.

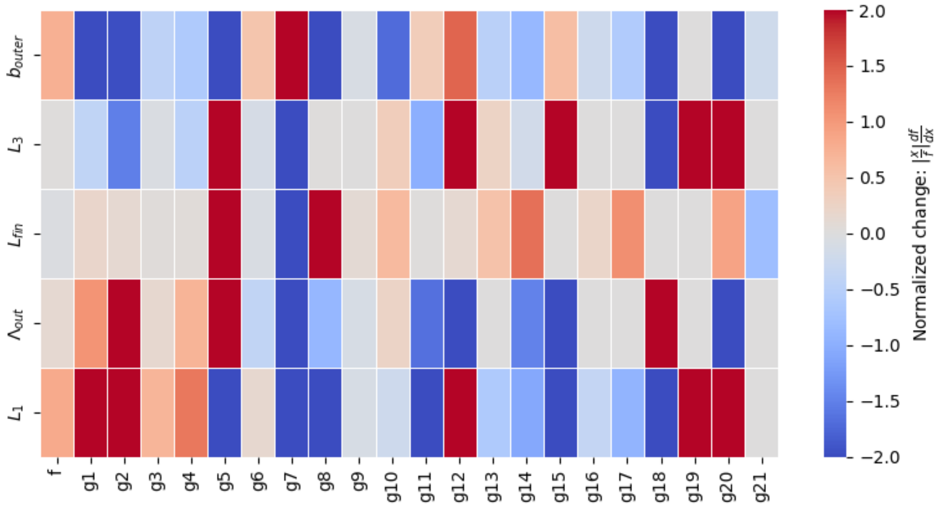

Figure 4.7: Sensitivity matrix. Objective function and constraints are on the x-axis, design variables are on the y-axis.

5

Results

5.1. Optimization Results

Before running the optimization, the objective function and constraints are evaluated for the initial design vector. The optimization is then performed two times. The first time, all constraints are included. The second time to see the effect of including stability and control constraints, only the geometric constraints were included. The results of the optimizations together with the initial design are presented in Table 5.1. It shows the design variables and resulting average fuel mass. A comparison of the planform geometry of the initial and optimized design is shown in Figure 5.1, accompanied by Table 5.2 which shows the differences in the main performance characteristics. A sideview comparison of the fin is shown in Figure 5.2. A topview of the three optimized family members is shown Figure 5.3. The normalized values of the constraints as calculated by Equation 3.4 and Equation 3.5 of the initial and optimized design vectors are shown in Figure 5.5 and Figure 5.6 using the numbering system of Table 3.4. The violated constraints can be recognised as the ones that are smaller than zero.

The initial design results into the highest average fuel mass. This fuel mass is the sum of design mission fuel and residual fuel. For the FV-800 and FV-900 all constraints are already satisfied. For the FV-1000, the steady sideslip and engine-out trim rudder power constraints are violated which is evident by constraint 5 and 8 being negative. All other stability and control constraints and all geometric constraints are satisfied. Thus, for the initial design 2 of the 63 constraints are violated.

The results of the first optimization where all constraints are taken into account are shown in the fourth column of Table 5.1. Overlays of the geometry of the initial and optimized FV-900 are shown in Figure 5.1 and Figure 5.2. The constraints corresponding to this design vector are shown in Figure 5.6. Due to the optimization, the average fuel weight has been reduced to 81637 kg, a reduction of 5 % compared to the initial design. The steady-sideslip and engine-out trim rudder power constraints are now satisfied due to the increased fin length from 7 to 9.05 m. This does not affect negatively affect other constraints too much, except the steady sideslip bank angle and the fin height which were not in danger of being violated. The untapered fuselage length of all three family members and outer wing span have decreased to reduce weight. The tapered part of the fuselage has increased in length, but the total fuselage is still shorter than in the initial design. The cargo and passenger space constraint is active for the FV-900 and FV-1000, preventing a shorter fuselage. The updated design variables have led to a lower maximum take-off weight and higher trimmed lift-to-drag ratio for all three family members, as can be seen in Table 5.2. The reduced weight can be attributed mainly to the shorter fuselage. Although the aspect ratio has not increased, the trimmed lift-to-drag is still higher than before the optimization. The position of the center of lift in cruise relative to the center of gravity may have improved such that smaller elevon deflections are required for trim. Also, the smaller wetted area contributes to lower skin friction drag and the larger fins could decrease vortex related induced drag. The outer wing sweep is decreased by five degrees. The decreased sweep can have a weight advantage, but could also compensate for the adverse effects of some design variable changes to some constraints. For example, the shorter outer wing span decreases the control power for take-off rotation since that elevon span has become smaller. The smaller sweep angle decreases the angle between the elevon hinge line and incoming flow, making it more effective. The longitudinal stability constraint for the FV-900 is almost active as it is close to zero, indicating that the aft-most CG is relatively close to the low-speed neutral point.

Another optimization is done without applying the stability and control constraints. This leads to only a 0.85 % smaller fuel weight compared to the more constrained optimization. Interestingly, the lengths L_1 and L_3 are different compared to first optimization, but the total length of the fuselage and wing shape is similar as can be seen in Figure 5.4. The inclusion of stability and control constraints into the optimization does not lead to a very different planform and the effect on fuel weight is small.

Design variables	Symbol	Initial design [3]	Optimized with S&C constraints	Optimized without S&C constraints
Outer wing span [m]	b_{outer}	14.75	13.87	15.20
Tapered fuselage length [m]	L_3	11.0	12.17	8.85
Fin length [m]	L_{fin}	7.0	9.05	8.44
Outer wing sweep [°]	Λ_{out}	40.7	34.97	35.48
Untapered fuselage length FV-800 [m]	$L_{1_{800}}$	18.0	15.84	17.21
Untapered fuselage length FV-900 [m]	$L_{1_{900}}$	24.0	21.5	23.65
Untapered fuselage length FV-1000 [m]	$L_{1_{1000}}$	29.0	26.40	28.40
Average fuel mass [kg]	$W_{\text{F}_{\text{avg}}}$	85931	81637	80947

Table 5.1: Flying-V family optimization results with design variables and fuel mass.

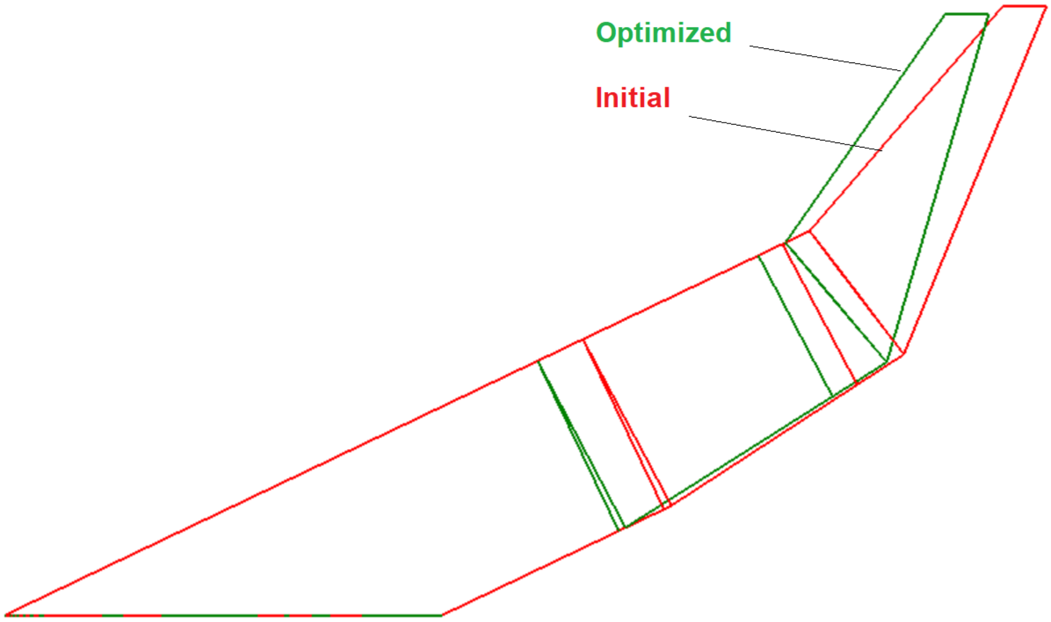

Figure 5.1: Overlay of initial and optimized design with stability and control constraints. Topview of FV-900.

	FV-800		FV-900		FV-1000	
	Initial	Optimized	Initial	Optimized	Initial	Optimized
$\frac{L}{D}$ (trimmed in cruise)	20.3	21.2	21.1	21.9	21.4	22.1
W_{F} [10^3 kg]	62.1	59.0	91.9	86.8	103.9	99.1
W_{MTO} [10^3 kg]	189.5	185.3	237.4	230.4	264.7	257.7

Table 5.2: Performance characteristics of the FV family for initial and optimized designs.

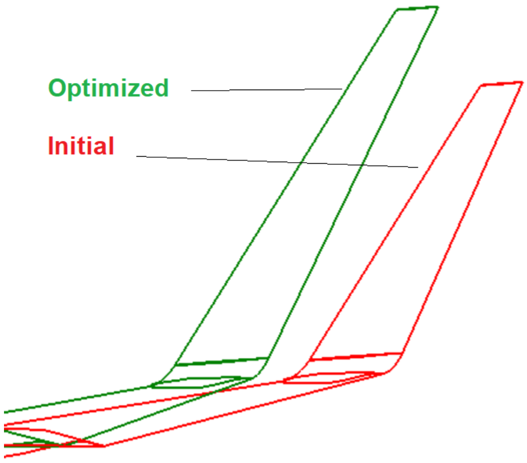
Optimized
Initial

Figure 5.2: Overlay of initial and optimized design with stability and control constraints. Sideview of fins.

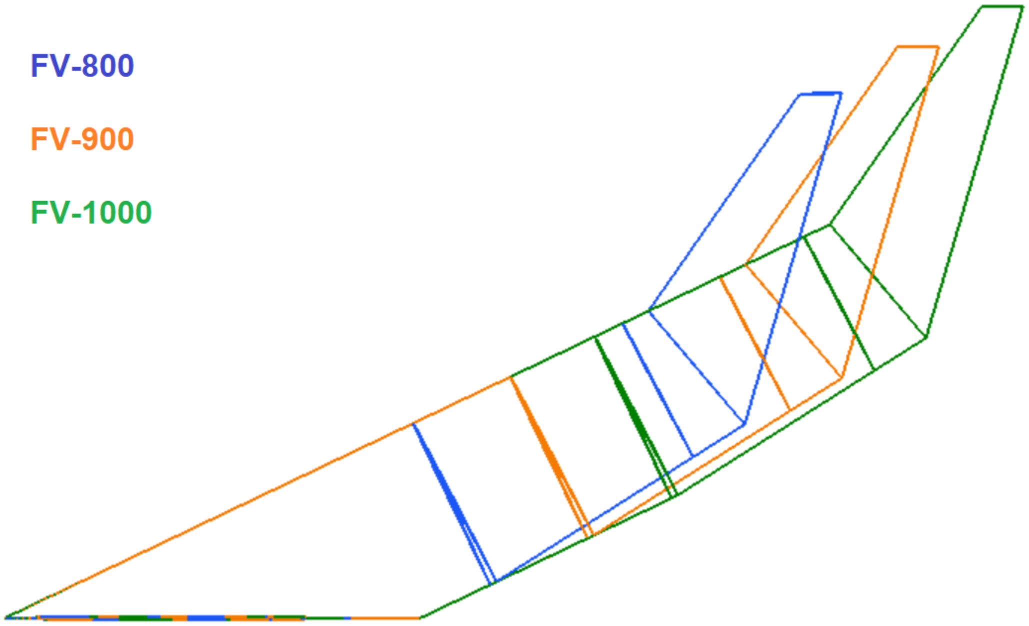
FV-800
FV-900
FV-1000

Figure 5.3: Optimized design of FV family with stability and control constraints.

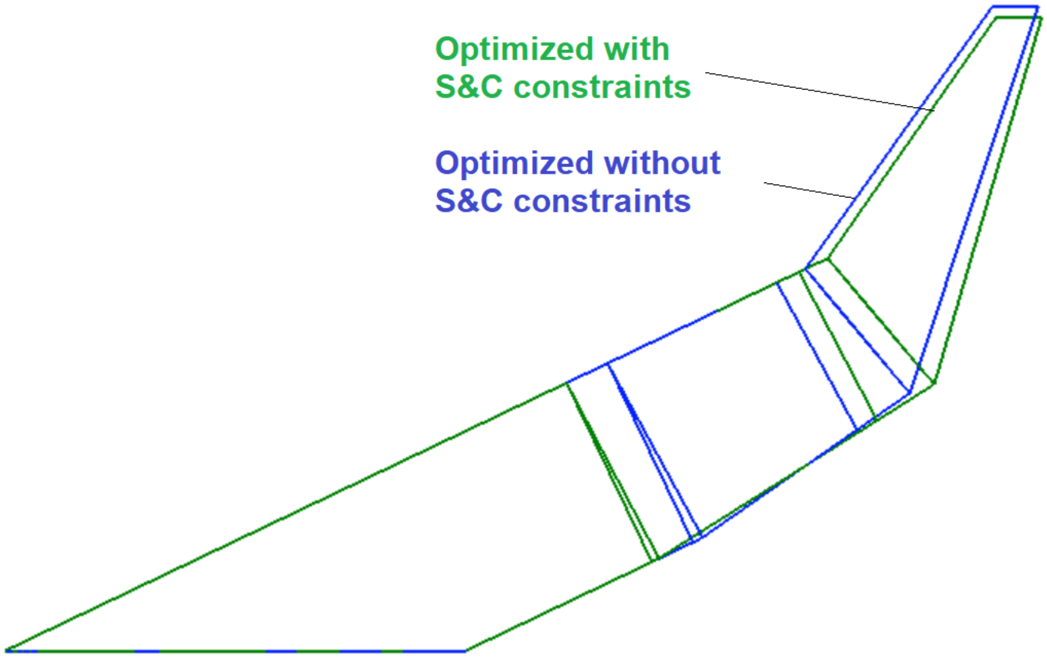

Figure 5.4: Overlay of optimized designs with and without stability and control constraints. Topview of FV-900.

5.2. Effect of Loading Scenario

The previous results have been obtained for a fixed design case of passenger and cargo loading. The design payload weight is distributed between passengers and cargo with a ratio of 84:16. The variation in center of gravity considered by the optimizer is therefore only caused by fuel weight variation. The range of center of gravity locations where all constraints are satisfied can be determined. For a certain combination of passenger and cargo loading, it should be checked whether the resulting CG is inside this safe range.

To discover in which range of center of gravity the constraints are satisfied, the constraints are plotted in Figure 5.7, Figure 5.8, Figure 5.9 for the FV-800, FV-900, and FV-1000 respectively. Lines are drawn for the constraints that are violated at a certain range of center of gravity location. If the constraint is larger than zero, the constraint is satisfied. Using the figure, the range of center of gravity in which all constraints are satisfied can be derived. In this range all lines are above the zero axis. For all three aircraft, the forward limit of CG is imposed by the longitudinal elevon control power for trim and the aft limit is imposed by longitudinal stability. The widths of the safe range of CG are 2.5 m for the FV-800 and FV-900 and 2.8 m for the FV-1000.

The FV-900 is used for the following example. The safe range of CG for the optimized FV-900 is between 25.0 and 27.5 m from the datum. Two loading scenarios and resulting center of gravity are shown in Table 5.3. In both cases the total weight adds up to the maximum take-off weight. The corresponding loading diagrams are shown in Figure 5.10 and Figure 5.11. In these figures the range of CG occurring during flight can be found. In the second case, the forward center of gravity of 24.7 m is outside the feasible range between 25.0 and 27.5 m. The combination of passenger and cargo loading leads to a too far forward CG at low fuel weight. It can be concluded that for each family variant there a range of CG in which there is sufficient stability and control, but a CG within this range is not guaranteed in every loading configuration. When the latter is the case, extra ballast in the passenger or cargo compartment may bring the CG within the acceptable range.

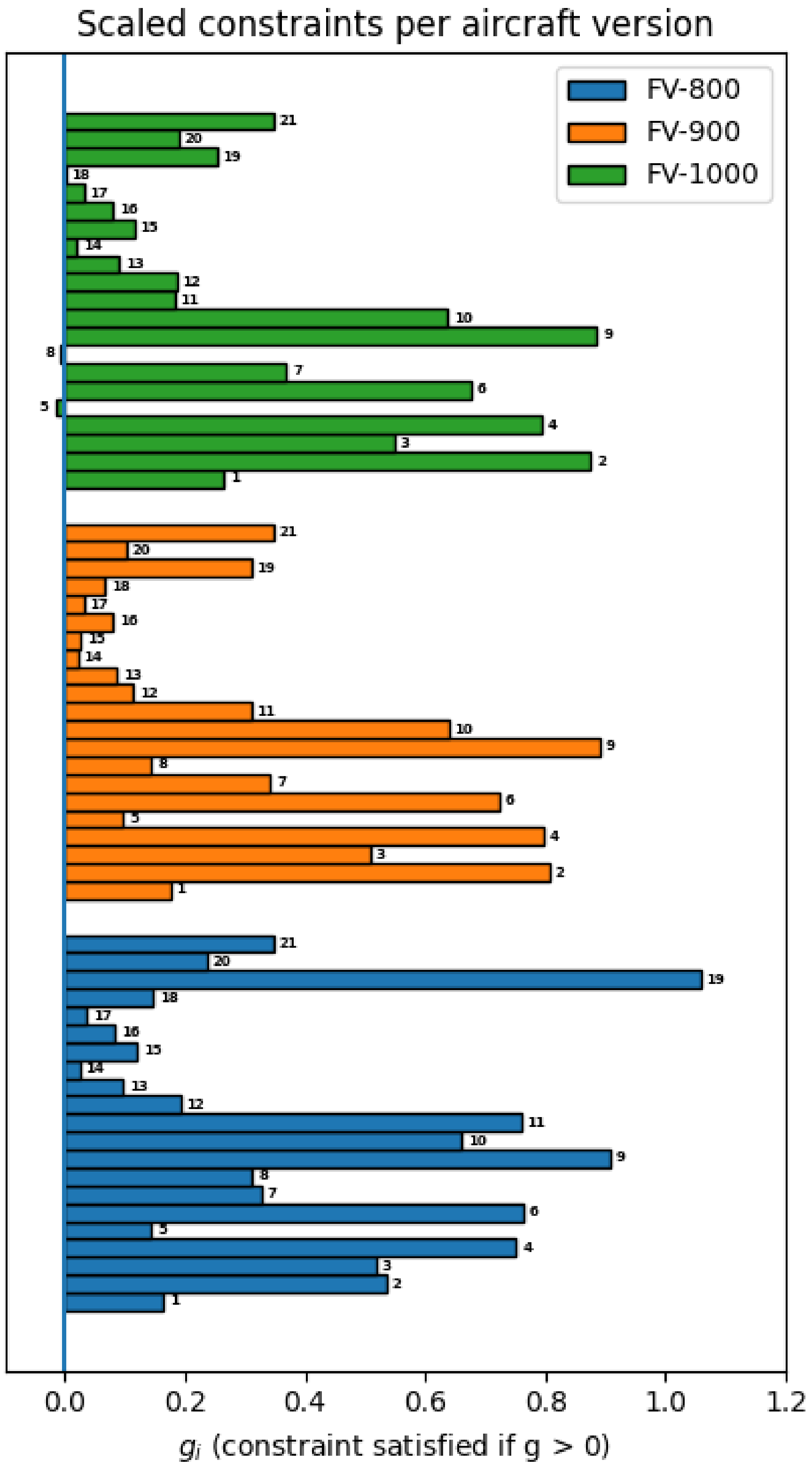

Figure 5.5: Constraints compliance and violation of initial design. Constraint values defined in Equation 3.4 and Equation 3.5.

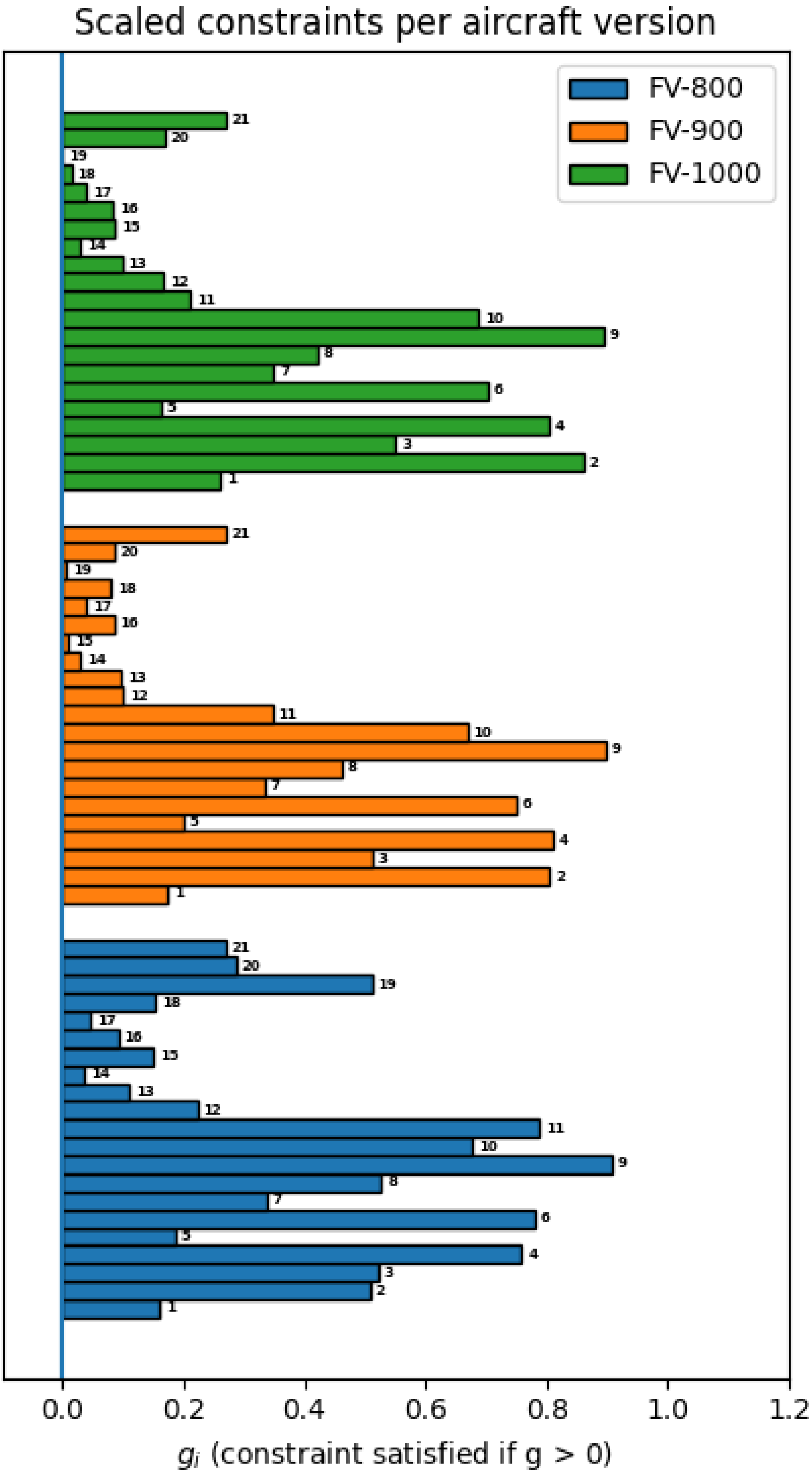

Figure 5.6: Constraints compliance and violation of optimized design with stability and control constraints. Constraint values defined in Equation 3.4 and Equation 3.5.

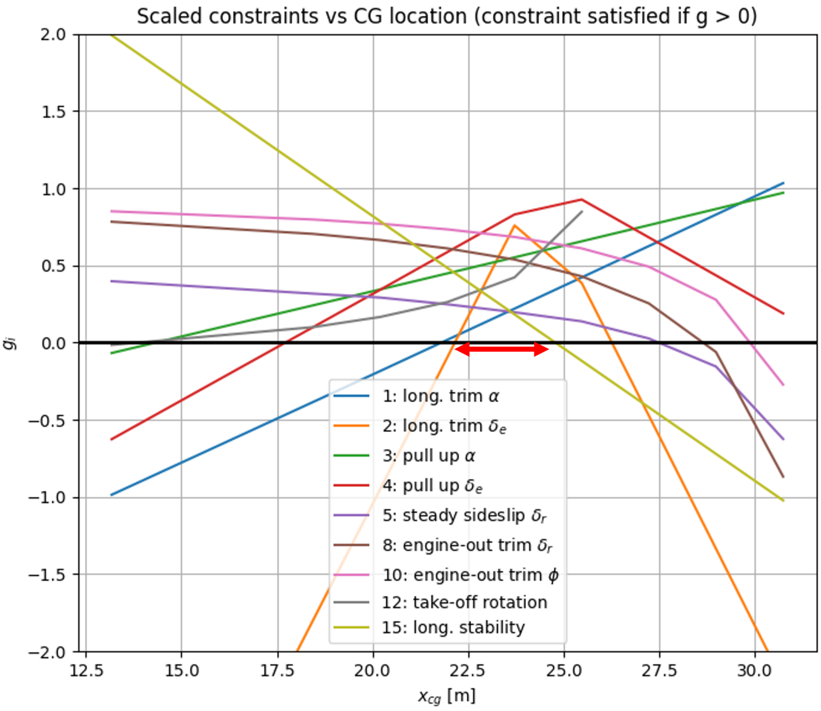

Figure 5.7: FV-800: Scaled constraints evaluated at a range of CG. Feasible range of CG indicated by red double arrow.

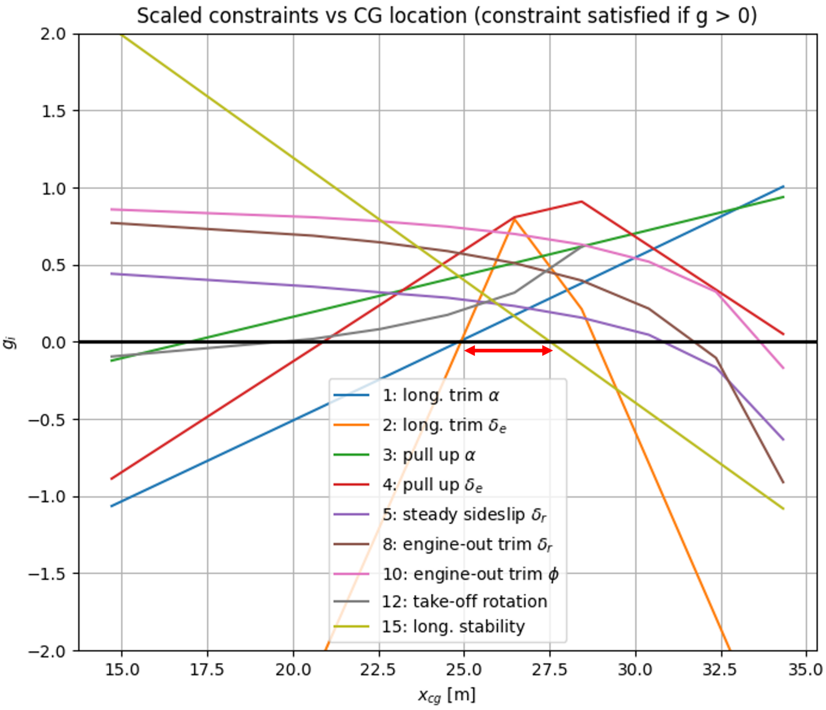

Figure 5.8: FV-900: Scaled constraints evaluated at a range of CG. Feasible range of CG indicated by red double arrow.

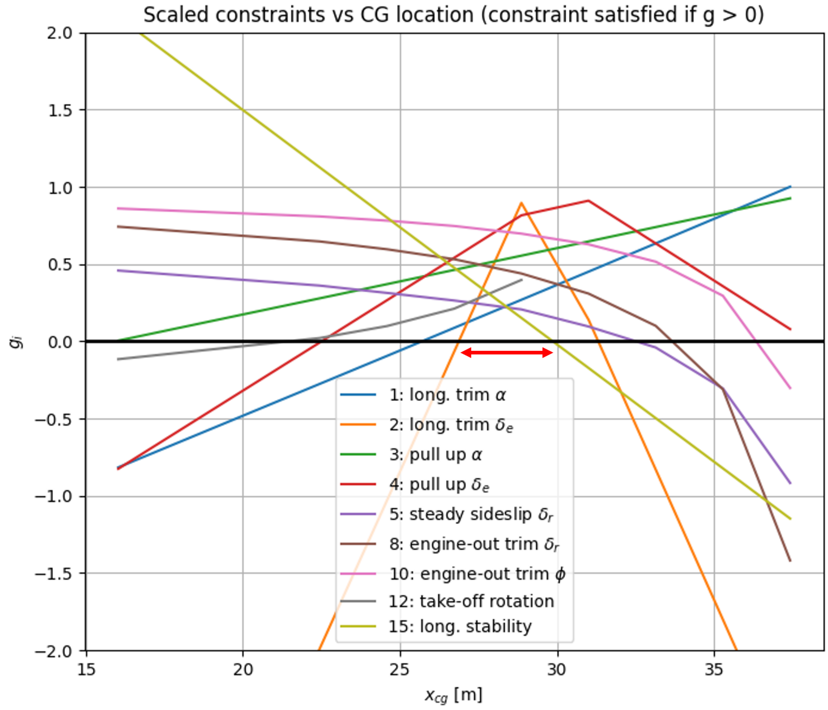

Figure 5.9: FV-1000: Scaled constraints evaluated at a range of CG. Feasible range of CG indicated by red double arrow.

	Case 1 (design case)	Case 2
$W_{\text{passengers}}$ [10^3 kg]	25.9	29.8
W_{cargo} [[10^3 kg]	4.9	1.0
W_{fuel} [[10^3 kg]	86.8	86.8
x_{cg} range in flight [m], see Figure 5.10 and Figure 5.11	25.2 - 27.4	24.7 - 27.1

Table 5.3: Center of gravity of the optimized FV-900 for different loading combinations. In all cases the passengers and cargo are concentrated in the back of their compartments and the fuel is distributed using the system explained in section 3.4.

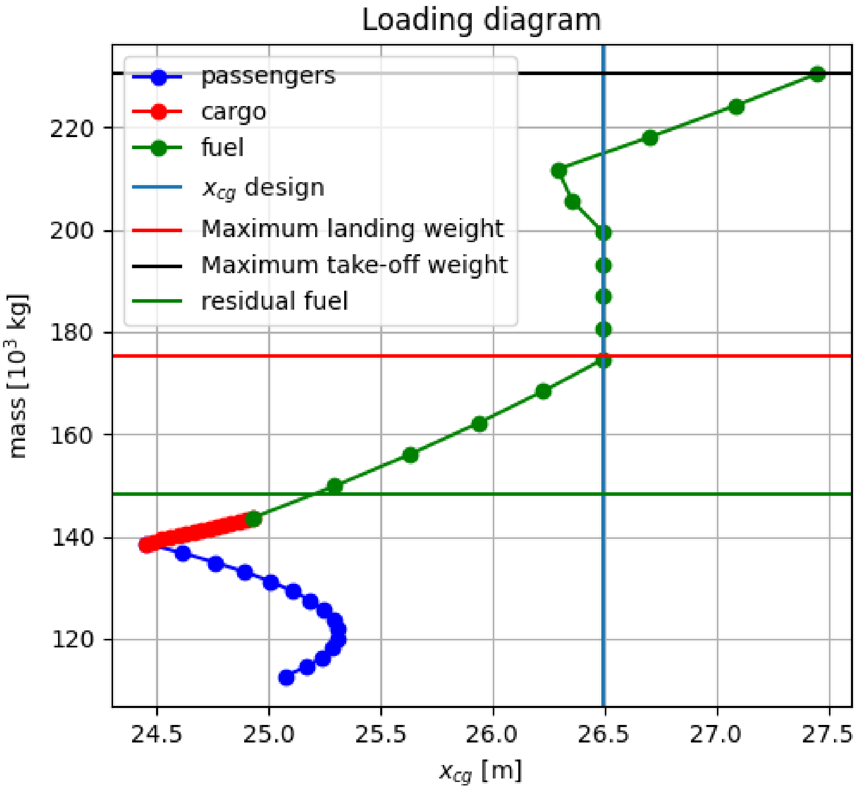

Figure 5.10: Loading diagram of the optimized FV-900 loaded as described by Case 1 in Table 5.3.

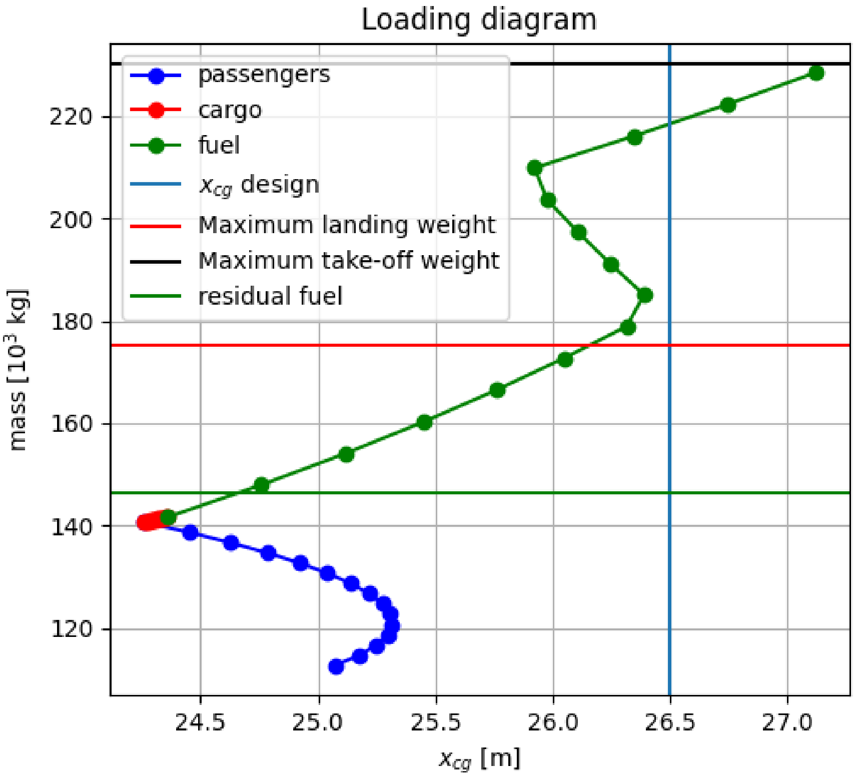

Figure 5.11: Loading diagram of the optimized FV-900 loaded as described by Case 2 in Table 5.3.

6

Conclusions and Recommendations

6.1. Conclusions

The goal of this thesis was to investigate the effect of stability and control constraints on the fuel burn performance and geometry of the Flying-V family consisting of three variants. To this end, an accurate mass distribution model was required that determines the moment of inertia and center of gravity in all possible payload and fuel loading scenarios. Using the modern tools of computer aided design and knowledge based engineering, the completion of this task was a straightforward process. In addition to this, it was shown that a system of active CG control by fuel distribution could reduce center of gravity movement during flight. The key elements to unlock insight into the stability and control behaviour of an aircraft are the stability and control derivatives. They can be used to simulate the motion of the airplane for varying control surface deflections. The stability and control derivatives depend not only the center of gravity location, but also on the aerodynamics around the aircraft. The vortex lattice solver *VORLAX* has proven be a valuable instrument for the fast evaluation of the aerodynamic forces and moments acting on the plane. Due to the simplifying assumptions inherent to potential flow solvers, the results should not be blindly trusted. Fortunately, research has been done recently on a scaled flight test model of the Flying-V that resulted in an identified aerodynamic model to which the solver's results could be compared. The lift slope and lift due to elevon was predicted accurately by the solver. Other derivatives like the rolling and yawing control power were overestimated. The comparison between the results of the flight test and the computed results has provided a way to derive correction factors for the stability and control derivatives that aim to include the effects not captured by the vortex lattice solver, such as thickness and boundary layer.

The optimization for fuel burn showed that the stability and control constraints do not impose a large penalty on the fuel burn performance of the Flying-V family. Most stability and control requirements are easily met. The only constraints violated by the initial design, the rudder power for steady sideslip and engine-out trim, could be repaired by increasing the fin length without much penalty on other constraints or the objective function. The stability and control constraints are not active in the optimization for fuel weight. Rather, the design space is constrained by geometric considerations like required cargo and passenger space. Compared to the initial design, the average fuel weight was reduced by 5 % after the optimization. The total length of the cabin was reduced by 1 m, 1.33 m, and 1.43 m for the FV-800, FV-900, and FV-1000 respectively. The fin length was increased by 2 m. The outer wing sweep angle has become about 5 degrees smaller. This change in design variables led to a higher trimmed lift-to-drag ratio and lower maximum maximum take-off weight, both contributing to reduced fuel burn in all three family variants. For example, the trimmed lift-to-drag ratio in cruise of the FV-1000 increased from 21.4 to 22.1, and the maximum take-off weight reduced from 264.7 tonnes to 257.7 tonnes. This led to design fuel weight reduction from 103.9 to 99.1 tonnes.

While looking in more detail into the effect of the center of gravity location, the main constraining requirements were found to be related to longitudinal stability and control. Depending on the combination of cargo, passenger, and fuel loading, the longitudinal trim control power or the longitudinal stability constraint could become active. The ranges of safe center gravity were found to have a width between 2.5 and 2.8 m for the three aircraft. Thus, a Flying-V family design is possible that is both fuel efficient and feasible in terms of stability and control. However, the aircraft must be loaded in a way that the center of gravity stays within the allowed range to guarantee stability and control during the flight.

6.2. Recommendations

Several recommendations for further research are proposed in this section.

In this research the left and right elevons both move the same number of degrees for roll control, creating a small difference in drag on both wing halves. The adverse yaw that this produces could be reduced by including a system of differential aileron deflection.

The elevon was assumed to consist of one large surface. More efficient controls may be achieved separating the elevon into multiple surfaces and designing a control allocation system that calculates the optimal combination of control surface deflections of the elevons and rudders for maneuvers and trim.

Due to the constraints on the computational power, a relatively simple aerodynamic model was used. More accurate modelling of the stability and control behaviour can be achieved by for example Euler equations or a RANS simulation. This could also affect the optimization results.

Even with a system of active CG control, the difference between most forward and aft CG can still be quite large depending on the loading of passengers and cargo. A new design of the fuel tanks which places them closer to the center of gravity of the empty aircraft could make the difference in CG smaller.

Effect that have not been considered in this research like aeroelastic effects and dynamic considerations could be included in a similar project to investigate their effect on fuel burn performance.

The optimization results suggests that quite a large fin length is needed for directional control. The tools used in this study do not take into account the structural and aeroelastic considerations that might negatively impact the feasibility of this. Other yaw control methods, like split rudders may be more appropriate than much larger fins.

More design variables can be added to the optimization than has been done here. It is conceivable that for example an increased root chord could increase the size of the inboard fuel tank, bring the total CG of the fuel closer to the empty CG, expanding the allowed passenger and cargo weight combinations.

In this research it was assumed that the aircraft is always loaded the same way in the two wing halves such that the center of gravity is on the symmetry plane (the XZ-plane). The effect of a weight difference that puts the center of gravity at a spanwise distance from the center could be investigated.

The design of the control system or avionics was not a part this thesis. The control system could be designed around the natural instability (in some cases) of the aircraft, for example a stability augmentation system to provide artificial stability. The mass distribution tool created for this research can still be used for center of gravity and moment of inertia estimation in further studies.

Bibliography

[1] J. Benad. The Flying V A New Aircraft Configuration for Commercial Passenger Transport. *Deutscher Luft- und Raumfahrtkongress*, 2015.

[2] R. Viet. Analysis of the Flight Characteristics of a Highly Swept Cranked Flying Wing by Means of an Experimental Test. *Master's thesis, Delft University of Technology*, 2019.

[3] W. Oosterom. Flying-V Family Design. *Master's thesis, Delft University of Technology*, 2021.

[4] N. Johnson. Effect of Winglet Integration and Rudder Deflection on Flying V Aerodynamic Characteristics. *Master's thesis, Delft University of Technology*, 2021.

[5] T. Cappuyns. Handling Qualities of a Flying V Configuration. *Master's thesis, Delft University of Technology*, 2019.

[6] A. Ruiz García, M. Brown, D. Atherstone, N. Arnhem, and R. Vos. Aerodynamic Model Identification of the Flying V from Sub-Scale Flight Test Data. In *AIAA Science and Technology Forum and Exposition, AIAA SciTech Forum 2022*, 2022.

[7] J. Wood and S. Bauer. Flying Wings / Flying Fuselages. In *39th AIAA Aerospace Sciences*, 2001.

[8] A. L. Bolsunovsky, N. P. Buzoverya, B. I. Gurevich, V. E. Denisov, A. I. Dunaevsky, L. M. Shkadov, O. V. Sonin, A. J. Udzhuhu, and J. P. Zhurihin. Flying wing - Problems and decisions. *Aircraft Design*, 4(4):193–219, 2001.

[9] R. H. Liebeck. Design of the Blended Wing Body Subsonic Transport. *Journal of Aircraft*, 41(1):10–25, 2004.

[10] N. Qin, A. Vavalle, A. Le Moigne, M. Laban, K. Hackett, and P. Weinerfelt. Aerodynamic considerations of blended wing body aircraft. *Progress in Aerospace Sciences*, 40(6):321–343, 2004.

[11] F. Faggiano. Aerodynamic Design Optimization of a Flying V Aircraft. *Master's thesis, Delft University of Technology*, 2016.

[12] L. van der Schaft. Development, Model Generation and Analysis of a Flying V Structure Concept. *Master's thesis, Delft University of Technology*, 2017.

[13] M. Claeys. Flying V Reference Aircraft Structural Analysis and Mass Comparison. *Master's thesis, Delft University of Technology*, 2018.

[14] B. Rubio Pasqual. Engine-Airframe Integration for the Flying-V. *Master's thesis, Delft University of Technology*, 2018.

[15] G. Bourget. The effect of landing gear implementation on flying v aerodynamics , stability and controllability. *Master's thesis, Delft University of Technology*, 2020.

[16] M. Palermo. The Longitudinal Static Stability and Control Characteristics of a Flying V Scaled Model. *Master's thesis, Delft University of Technology*, 2019.

[17] M. Hillen. Parametrisation of the Flying-V Outer Mould Line. *Master's thesis, Delft University of Technology*, 2021.

[18] J. Horwitz. Parametric design of the Flying-V Winglets for Improved Lateral-Directional Stability and Control. *Master's thesis, Delft University of Technology*, 2021.

[19] G. La Rocca. Advanced Engineering Informatics Knowledge based engineering: Between AI and CAD. Review of a language based technology to support engineering design. *Advanced Engineering Informatics*, 26:159–157, 2021.

[20] J. D. Anderson. *Fundamentals of Aerodynamics*. McGraw Hill, 1984.

[21] F. M. White. *Viscous Fluid Flow*. McGraw Hill, 2006.

[22] L. R. Miranda, R. D. Elliot, and W. M. Baker. A Generalized Vortex Lattice Method for Subsonic and Supersonic Flow Applications. *NASA CR 2865*, 1977.

[23] T. J. Souders and T. T. Takahashi. VORLAX 2020: Benchmarking Examples of a Modernized Potential Flow Solver. *AIAA 2021-2459*, 2021.

[24] D. P. Raymer. *Aircraft Design: A Conceptual Approach*. American Institute of Aeronautics and Astronautics, 1999.

[25] E. Torenbeek. *Synthesis of Subsonic Airplane Design*. Delft University Press, Delft, 1982.

[26] K. Schmidt and R. Vos. A semi-analytical weight estimation method for oval fuselages in conventional and novel aircraft. In *52nd Aerospace Sciences Meeting*, 2014.

[27] A. Elham, G. La Rocca, and M. J. L. Van Tooren. Development and implementation of an advanced, design-sensitive method for wing weight estimation. *Aerospace Science and Technology*, 29(1):100–113, 2013.

[28] *Certification Specifications for Large Aeroplanes CS-25 - Amendment 26*. European Union Aviation Safety Agency.

[29] Jan Roskam. *Airplane Design: Part VII: Determination of Stability, Control and Performance Characteristics: FAR and Military Requirements*. University of Kansas, Lawrence, Kansas, 2006.

[30] J. Kay, William Mason, W. Durham, F. Lutze, and A. Benoliel. Control Authority Issues in Aircraft Conceptual Design: Critical Conditions, Estimation Methodology, Spreadsheet Assessment, Trim and Bibliography. 03 2012.

[31] B. Etkin. *Dynamics of Flight*. John Wiley Sons, Inc., 1976.

[32] M. Anyoji, M. Okamoto, H. Hidaka, K. Kondo, A. Oyama, H. Nagai, and K. Fujii. Control surface effectiveness of low Reynolds number flight vehicles. *Journal of Fluid Science and Technology*, 9(5), 2014.